

The Optimal State for Gravity Currents in Shear

GEORGE H. BRYAN AND RICHARD ROTUNNO

National Center for Atmospheric Research, Boulder, Colorado*

(Manuscript received 29 May 2013, in final form 2 August 2013)

ABSTRACT

This study examines the lifting of sheared environmental air by gravity currents, focusing primarily on the theoretical “optimal state” in which near-surface flow is turned into a vertically oriented jet. Theoretical models are presented from multiple perspectives, including the vorticity perspective that was first presented by Rotunno, Klemp, and Weisman and a flow-force balance perspective based on conservation of mass and momentum. The latter approach reveals a constraint on the depth of the environmental shear layer relative to the depth of the cold pool. Based on these control-volume constraints, a numerical solution for steady, inviscid, isentropic flow is obtained that shows how the cold-pool interface has a slightly concave shape and is nearly (although not strictly) vertical. Then, by initializing a time-dependent numerical model with a stagnant cold pool in an environment with low-level shear, it is shown that a statistically steady flow can be maintained with all the important elements of the analytic solution. Most notably, the front-relative flow is negligible behind the surface gust front at all levels, the interface of the cold pool maintains a predominantly vertical structure, and the net generation of vorticity by buoyancy within a control volume closely matches the horizontal flux of environmental vorticity on the side of the control volume. Sensitivity simulations confirm that the constraints identified by the analytic study must be met for the optimal state to be realized and that lifting of near-surface environmental air is optimized when a vertically oriented jet is created and maintained.

1. Introduction

Cold-air outflows play an important role in many midlatitude convective storms and convective storm systems. These outflows, being denser than their environments, spread under the influence of gravity and have long been identified with the “gravity current” phenomenon (Simpson 1997). The basic gravity current analysis considers a mass of denser air moving steadily along the lower surface toward less dense air contained in a channel (Ungarish 2009). Assuming a free-slip condition at the lower and upper boundaries, it is customary to consider the equivalent problem of a stationary denser air mass overrun by a less dense air mass of constant speed, for which constraints on the depth and propagation speed of the gravity current can be determined (Benjamin 1968).

The other important contributor to the dynamics of midlatitude convective storms and systems thereof is the variation of the horizontal wind with height (or “vertical wind shear”) over the first several kilometers above ground level (e.g., Rotunno et al. 1988, hereafter RKW). The distinctive behavior of thunderstorm cold-air outflows in vertical wind shear was identified in the numerical simulation study of RKW where it was observed that cold-air outflows produce much deeper lifting of the environmental warm air mass when the direction of the outflow is the same as the vertical wind shear vector; the lifting was found to be greatest for a certain value of vertical wind shear magnitude. RKW further noted that vertical wind shear adds a separate and nontrivial dynamical element to be considered in the behavior of gravity currents and offered an explanation of this behavior in terms of the horizontal component of vorticity directed along the density contrast. In particular, RKW hypothesized that for a given cold air mass there exists an optimal value of shear that allows the inflow layer to be turned to the vertical, which then separates from the gravity current leading edge and flows upward without limit in the presumed unstratified environment. While all subsequent studies confirm the basic RKW

*The National Center for Atmospheric Research is sponsored by the National Science Foundation.

Corresponding author address: George H. Bryan, NCAR, 3090 Center Green Dr., Boulder, CO 80301.
E-mail: gbryan@ucar.edu

conclusion that environmental vertical wind shear can produce deeper lifting by a gravity current, some studies have raised questions concerning the RKW vorticity-based theory in general and the above-described “optimal” state in particular. The present work addresses these questions.

Prior to RKW only two studies of the effects of environmental shear existed in the gravity current literature (Rottman et al. 1985; Jirka and Arita 1987). Both studies found through theoretical analysis that vertical shear in the direction of gravity current motion should produce a more vertical flow at the leading edge of the gravity current; these results were experimentally confirmed in the laboratory. The theoretical analysis by Rottman et al. (1985) found that the leading edge of the gravity current makes an angle of $\pi/3$ with the lower surface irrespective of the environmental shear; however, above the lower surface the leading-edge slope was predicted to increase with shear. These results were reinforced by the theoretical and numerical calculations of Xu (1992).

Following the classic analysis of gravity currents in a confined channel by Benjamin (1968), Xu (1992) considered the effects of constant ambient shear through the entire channel. Assuming free-slip conditions at the upper and lower surfaces, the vertically integrated pressure-corrected horizontal momentum flux (the “flow force”) is the same at large distances upwind and downwind from the gravity current leading edge for steady flow; together with the hydrostatic equation at these distances, an equation is derived for the speed of the current in terms of the acceleration due to gravity, the density difference, the height of the gravity current downwind, and its ratio to the height of the channel. Xu (1992) found that the downwind height of the gravity current increases as shear increases and, by implication, the leading-edge slope of the gravity current (away from the lower surface) must increase with shear. Since the horizontal vorticity equation is not directly used in Xu’s analysis, Xu and Moncrieff (1994, p. 444) speculated on the possibly different roles played by “vorticity balance” as envisioned by RKW and “flow-force balance” in the dynamics of gravity currents in shear.

Hovering in the background of such discussions is the fact that the models used in previous flow-force approaches preclude the possibility of inflow–airflow separation from the leading edge of the gravity current, which is fundamental to the RKW optimal state. In fact, a recent study (Davies-Jones and Markowski 2013, p. 1209) concludes that the RKW vorticity budget “seems impossible” for inviscid adiabatic flow; a similar conclusion was reached by Xu (1992, p. 523). A secondary but nonetheless significant difference of the flow-force approaches to the RKW optimal state is the important

role played by the upper lid, which would obviously prohibit a vertically oriented jet. Actually, the discussion section of Xu (1992) acknowledged that a rigid upper boundary condition was perhaps “too restrictive” and suggested that further investigation was warranted.

In the present work we revisit the RKW optimal state for gravity currents in which a sheared environmental flow is turned into a vertically oriented jet and thus lifting of environmental air is optimized; hereafter this overall flow configuration, as illustrated in Fig. 1, is referred to simply as “the optimal state,” a term chosen by RKW to highlight the fact that lifting of environmental air is maximized for this flow configuration. We consider both vorticity and flow-force balances in the absence of a confining upper boundary. We find that the addition of the flow-force balance sets a previously unpublished condition on the height of the shear layer with respect to the height of the gravity current, but that otherwise the RKW optimal state is a theoretical possibility for both viscous and inviscid flows that satisfies both vorticity and flow-force balances. Following a technique similar to Xu et al. (1992), we also develop a numerical solution for steady, inviscid, isentropic flow that reveals the shape of the interface for a gravity current in the hypothesized RKW optimal state. Time-dependent turbulence-resolving numerical solutions are also presented that show that the RKW vertically oriented jet is a robust solution to the equations of motion.

2. Analytic study of the optimal state

a. Governing equations

Herein we consider two-dimensional flow (u, w) in Cartesian coordinates (x, z). The governing equations are the shallow Boussinesq momentum, temperature, and continuity equations (e.g., Ogura and Phillips 1962):

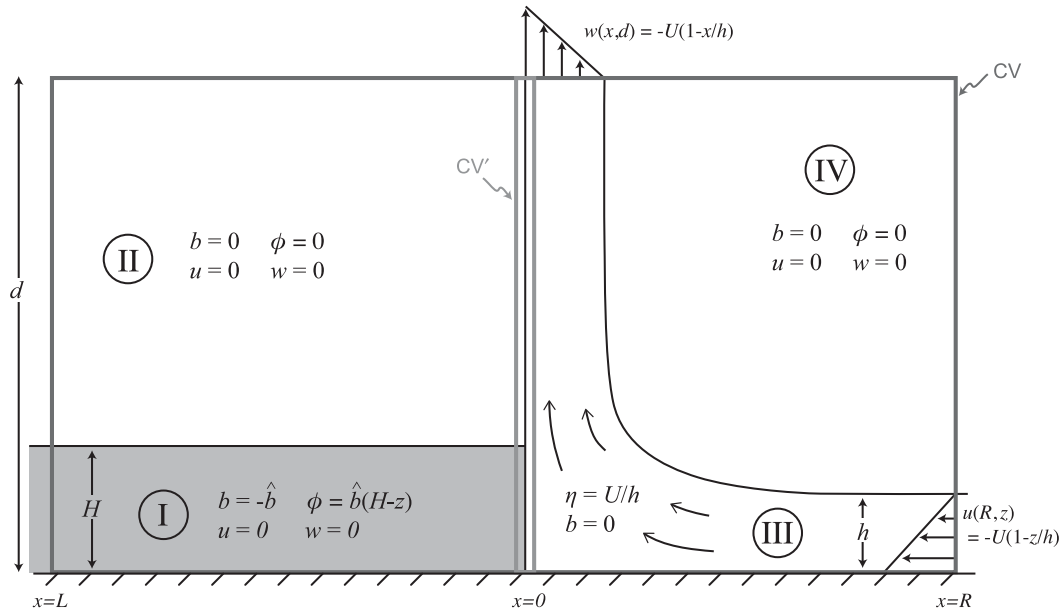
$$\frac{du}{dt} = -\frac{\partial\phi}{\partial x} + D^u, \tag{1}$$

$$\frac{dw}{dt} = -\frac{\partial\phi}{\partial z} + b + D^w, \tag{2}$$

$$\frac{db}{dt} = D^b, \tag{3}$$

$$\frac{\partial u}{\partial x} + \frac{\partial w}{\partial z} = 0, \tag{4}$$

where $d/dt = u\partial/\partial x + w\partial/\partial z$; $b = g\theta'/\theta_0$ is the buoyancy and θ' the perturbation potential temperature away from a constant reference θ_0 ; and the pressure variable $\phi = c_p\theta_0\pi'$, where the Exner function $\pi \equiv (p/p_0)^{R/c_p}$, p is the pressure, $p_0 = 1000$ hPa is a reference pressure, R is the



$$U = (2b\hat{H})^{1/2}, \quad h/H = 3/4$$

FIG. 1. Idealized schematic of the optimal state for a gravity current in a sheared environment.

dry-air gas constant, c_p is the specific heat at constant pressure, and g is the acceleration due to gravity. The diffusion terms D^u , D^w , and D^b are given by

$$D^u = \frac{\partial \tau_{xx}}{\partial x} + \frac{\partial \tau_{xz}}{\partial z}, \tag{5}$$

$$D^w = \frac{\partial \tau_{xz}}{\partial x} + \frac{\partial \tau_{zz}}{\partial z}, \tag{6}$$

$$D^b = -\frac{\partial F_x}{\partial x} - \frac{\partial F_z}{\partial z}, \tag{7}$$

where τ is stress and F is potential temperature flux. The diffusion terms may represent turbulent or laminar flow.

b. The RKW theory

The present topic is motivated by a discussion of the mechanisms by which sheared inflow may interact with a cold pool to produce deep lifting of the inflow air (and thereby initiate convective cells in environments with moisture). Taking advantage of the simplicity of the vorticity form of these equations in two dimensions allows (1), (2), and (4) to be replaced by

$$\frac{d\eta}{dt} = -\frac{\partial b}{\partial x}, \tag{8}$$

$$\nabla^2 \psi = \eta, \tag{9}$$

where $\eta = \partial u/\partial z - \partial w/\partial x$, $u = \partial \psi/\partial z$, $w = -\partial \psi/\partial x$, and $\nabla^2 = \partial^2/\partial x^2 + \partial^2/\partial z^2$. The viscous terms were neglected in RKW since in their simplest constant-viscosity (ν) form they contribute the term $\nu \nabla^2 \eta$ to the rhs of (8) and thus would have no impact on the qualitative arguments made in RKW (sections 4a and 4b). Those arguments are simply this: the flow associated with a cold pool in an unsheared ($\eta = 0$) environment has, by (8), $\eta < 0$ produced at the cold-air edge (RKW, their Fig. 18b) and, by (9), the induced flow is over the cold pool; when the environment (with $w = 0$) has shear $\partial u/\partial z = \eta > 0$, then by (9) the flow induced by the negative vorticity of the cold pool can be countered by flow induced by the positive environmental vorticity such that a greater vertical displacement of the inflow layer can be realized (RKW, their Fig. 18d). We note that the steady-state assumption is not needed, nor does potential temperature diffusion enter in this argument. We further note that the concept of an optimal state has not yet been introduced; that is, it is not an underlying part of RKW's theory.

c. The RKW quantitative criterion (vorticity balance)

To get an estimate of the shear that would produce the deepest lifting for a given cold pool, RKW examined the steady version of (8) in flux form; including the diffusion terms it is

$$\frac{\partial}{\partial x}(u\eta + b + D^w) + \frac{\partial}{\partial z}(w\eta - D^u) = 0. \quad (10)$$

Figure 1 presents a hypothetical optimally lifted sheared inflow based on the gravity-current-in-shear experiments from RKW (their Fig. 20) and subsequent studies (e.g., Weisman and Rotunno 2004, their Fig. 6). The hypothetical model has four distinct regions: 1) a stagnant [$(u, w) = 0$] cold pool of constant potential temperature deficit ($b = -\hat{b}$); 2) a neutral ($b = 0$) stagnant layer directly over the cold pool; 3) a neutral layer of constant positive vorticity with inflow velocity

$$u(R, z) = -U(1 - z/h) \quad (11)$$

entering from the lower-right side (with $w = 0$) and deflected upward at the cold-air edge; and 4) a neutral stagnant zone bounding the constant-vorticity layer on its upper-right side. Integration of (10) over a rectangular control volume (CV) centered on, and moving with, the leading edge of the cold pool (Fig. 1) gives

$$\int_0^d (u\eta + b + D^w)|_L^R dz + \int_L^R (w\eta - D^u)|_0^d dx = 0, \quad (12)$$

where d is the height at which the hypothesized flow becomes independent of z . In this case there is no contribution from the $w\eta$ term since $\eta \rightarrow -\partial w/\partial x$ as $z \rightarrow d$ and therefore the integral over x at $z = d$ is exactly zero, while at $z = 0, w = 0$. For the hypothesized flow (Fig. 1), there is no motion on the left side, and viscous and/or turbulent effects at the left and right sides of the CV are assumed negligible; hence, (12) simplifies to

$$\int_0^d u\eta|_R dz - \int_0^d b|_L dz - \int_L^R D^u|_0^d dx = 0. \quad (13)$$

The use of a free-slip lower boundary condition in the RKW experiments precludes the development of a boundary layer at $z = 0$ and it is straightforward to show that the diffusion term in (13) is $O(\text{Re}^{-1})$, where $\text{Re}^{-1} = \nu/UH$, and thus is negligible under normal atmospheric conditions. Application of the hypothetical model (Fig. 1) to (13) yields the estimate

$$U = \sqrt{2\hat{b}H}, \quad (14)$$

which is identical to RKW's (10). We note again that potential-temperature diffusion does not enter directly in arriving at (14).

The variable U in (14) represents both the propagation speed of the cold pool for the flow shown in Fig. 1 and the environmental wind difference over depth h

(i.e., Δu , a measure of environmental shear). The right-hand side of (14) is often represented by the variable c (e.g., RKW, p. 478) and is frequently interpreted as the "intensity" of a cold pool. We note that (14) is the "quantitative criterion" derived by RKW for the amount of shear needed to "balance" a cold pool (RKW, p. 477). The two sides of (14)—that is, $\Delta u = U$ from the left-hand side and $c = \sqrt{2\hat{b}H}$ from the right-hand side—have also been used in a more general way to quantify the effects of cold pools and shear on the structure and evolution of gravity currents and/or squall lines (e.g., Weisman et al. 1988; Weisman and Rotunno 2004), as discussed in section 5b herein.

We also note that (14) was derived using a linear wind profile, (11), but that the same result arises from any form of $u(z)$. We elaborate further in section 6.

Finally, we note that stagnant flow (relative to the surface gust front) does not need to be assumed for the cold pool (region I); see, e.g., Weisman (1992, p. 1839).

d. Flow-force balance

Analytical calculations of gravity currents in shear have been performed before but always in the presence of a confining horizontal upper boundary (e.g., Xu 1992), which admittedly is an unrealistic constraint in the present meteorological context (Xu et al. 1996, p. 785). A primary tool for analyzing gravity currents is an analysis of the vertically integrated horizontal momentum equation [(1)] in a frame of reference in which the speed of the current is steady:

$$\int_0^d (u^2 + \phi - \tau_{xx})|_L^R dz + \int_L^R (uw - \tau_{xz})|_0^d dx = 0. \quad (15)$$

Under the assumed conditions of $u \rightarrow 0$ as $z \rightarrow d$ and zero-stress conditions along the edges of the CV, (15) takes the same form as it does for gravity currents in a confined channel,

$$\int_0^d (u^2 + \phi)|_L^R dz = 0, \quad (16)$$

which is known as the flow-force balance (Benjamin 1968). Given the specifications of (u, w) and b at the edges of the CV (Fig. 1), it follows that

$$\phi(R, z) = 0, \quad \phi(L, z) = \begin{cases} \hat{b}(H - z) & \text{for } 0 \leq z \leq H \\ 0 & \text{for } H \leq z \leq d \end{cases}. \quad (17)$$

In (16), substituting (11) for u and (17) for ϕ gives the condition

$$U^2 = \frac{3\hat{b}H^2}{2h}. \quad (18)$$

The physical interpretation of (18) is that the column-integrated hydrostatic pressure in the cold pool matches the column-integrated horizontal momentum flux on the right side; in other words, the incoming horizontal momentum is “stopped” by the cold pool. When (18) is compared with (14), we find that

$$\frac{h}{H} = \frac{3}{4} \quad (19)$$

is required for flow-force balance. This previously unpublished constraint on the height of the shear layer with respect to the height of the gravity current is specific to the linear wind profile in (11). Other wind profiles yield different constraints, as discussed in section 6.

e. Optimal-state flow model

Up to this point no explicit use has been made of the hypothetical flow interior to the CV shown in Fig. 1, but rather the hypothetical conditions at the edges of the CV were used to arrive at integral constraints (14) and (18). In this section we propose an approximate model for the interior flow.

The main approximation is that the flow pictured in Fig. 1 is inviscid and adiabatic; with this approximation, it is easy to see that the steady, inviscid equations of motion [(1)–(4)] are satisfied for $x < 0$ [since $(u, w) = 0$ and $\phi(x, z)$ is given by hydrostatic balance as in (17)] and for $x > 0$ [since $b = 0$ and the steady, inviscid version of (8) is satisfied for η constant (region III) or $\eta = 0$ (region IV)]. The zero-diffusion approximation will of course break down near $x = 0$ since in any real fluid (and likely most numerical simulations) there are always small, but finite, viscosities and thermal diffusivities, and we expect effects of diffusion to be important at least within some small distance of the strong gradients in b and w at $x = 0$. However, the effect of the zero-diffusion approximation on the present analytical model predictions will be evaluated with numerical simulations including diffusion to be presented in a later section.

With the zero-diffusion approximation, (8) and (11) imply that $\eta = U/h$ throughout region III in Fig. 1; using this fact with (4), we find

$$w(x, d) = \begin{cases} 0 & \text{for } -\infty < x < 0 \\ U(1 - x/h) & \text{for } 0 < x \leq h \\ 0 & \text{for } h \leq x < \infty \end{cases} \quad (20)$$

for the outflow profile. The discontinuity of $w(x, d)$ at $x = 0$ implies $\eta(x, z = d) = -U\delta(x)$ at $x = 0$ where $\delta(x)$ is the delta function.

Leaving aside for the moment the stability of the discontinuous distribution $w(x, d)$, the basic question to be answered is how this distribution is generated by upstream conditions. To answer this question, we consider again the steady flux form of the vorticity equation as in (12), except here we focus on the infinitesimal volume enclosing the hypothetical cold-pool edge at $x = 0$ (CV' in Fig. 1). Here we make the second approximation of this analysis by assuming that the inflow streamline that borders the cold air is vertical so that $u(0, z) = 0$. The relevant equation is obtained from (12) by setting the limits $(L, R) = (0^-, 0^+)$ and $d = z$ and by setting $u = D^u = D^v = 0$, which gives

$$\int_0^z b|_{0^-}^{0^+} dz + \int_{0^-}^{0^+} w\eta|_0^z dx = 0, \quad (21)$$

and since $\eta = -\partial w/\partial x$ with $u(0, z) = 0$, (21) immediately yields

$$w^2(x = 0^+, z) = \begin{cases} 2\hat{b}z & \text{for } 0 \leq z \leq H \\ 2\hat{b}H & \text{for } H \leq z \leq d \end{cases}, \quad (22)$$

which is consistent with (20) since by (14), $U^2 = 2\hat{b}H$. We note for completeness that $\hat{b}H$ is the stagnation pressure at the origin.

The implication of the foregoing analysis is that the streamline at $x = 0$ undergoes a separation from the cold pool at $z = H$ and that the outflow vorticity

$$\eta(x, d) = -U\delta(x) \quad (23)$$

is produced at the interface between the cold air and neutral inflow stream, which is to say that b is constant within each fluid mass but has an infinite gradient between them. As mentioned above, we expect effects of diffusion to be important within some small distance of the strong gradients in b and w at $x = 0$ in actual (viscous) fluids and in our numerical model simulations (presented later). However, as we shall see in a later section, the main prediction of the model—that there is a statistically steady vertically oriented jet when (14) and (19) are satisfied—is well supported by numerical simulations.

f. A numerical solution for steady, inviscid, adiabatic flow

To add further credence to the hypothetical model shown in Fig. 1, we develop here a numerical solution for $\psi(x, z)$ assuming the right edge of the cold pool is a free interface and that the flow is steady, adiabatic, and inviscid. Our solution procedure uses the same dynamical constraints as analogous studies by Xu et al. (1992) and

Xu (1992, his section 3). The primary difference is conceptual: rather than assuming flow in a confined channel with $w = 0$ along an upper boundary [as shown in the first figure of both Xu et al. (1992) and Xu (1992)], we instead assume flow as shown in Fig. 1 with separation of flow from the interface (i.e., from the cold pool) at height H , an inflow profile given by (11), and an outflow profile given by (20).

Our solution is obtained in two steps. For step 1 we determine the shape of the free interface between regions III and IV; for step 2 we determine the shape of the free interface between regions I and III. For both steps we determine a solution by iteration wherein the shape of the free surface is changed in small increments until a solution for $\psi(x, z)$ is found that satisfies a set of boundary conditions and where the flow satisfies (9) at every grid point.

For step 1, we assume a perfectly vertical interface between regions I and III, for which a consistent distribution of η is given as follows:

$$\eta(x, z) = \begin{cases} 0 & \text{for } L \leq x < -\Delta, 0 \leq z \leq d \\ -\sqrt{2\hat{b}z}/\Delta & \text{for } -\Delta \leq x < 0, 0 \leq z \leq H \\ -\sqrt{2\hat{b}H}/\Delta & \text{for } -\Delta \leq x < 0, H \leq z \leq d \end{cases} \quad (24)$$

The final line of (24) is the same as (23), except here we recognize there is a finite grid spacing Δ . Boundary conditions also include $w(L, z) = w(R, z) = w(x, 0) = 0$ and $u(L, z) = u(x, d) = 0$ with $\psi(L, z) = \psi(x, 0) = 0$. The initial distribution of environmental vorticity η on the grid interior is given as

$$\eta(x, z) = \begin{cases} \sqrt{2\hat{b}H}/h & \text{for } 0 \leq x \leq R, 0 \leq z \leq h, \\ \sqrt{2\hat{b}H}/h & \text{for } 0 \leq x \leq h, 0 \leq z < d, \end{cases} \quad (25)$$

and is zero otherwise. The iterative procedure for step 1 slightly perturbs the shape of the interface between regions III and IV; specifically the interface defined by $\eta = 0$ on one side, and $\eta = \sqrt{2\hat{b}H}/h$ on the other side, is moved slightly during each iteration. Using (9), a solution for $\psi(x, z)$ is determined each step, which then determines $u(x, z)$ and $w(x, z)$. We then check for consistency between ψ and Bernoulli energy E along the free interface, both of which are constant and known (via the specified boundary conditions). When the error in ψ and E exceed some threshold value, the interface is moved by one grid point (either up/down or left/right depending on

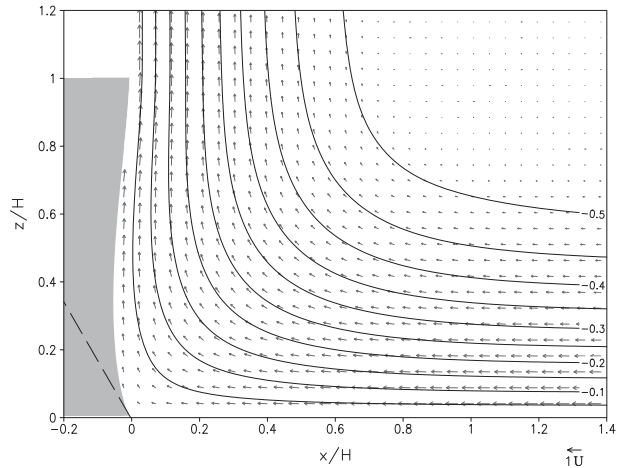


FIG. 2. Numerical solution for the optimal state assuming steady, inviscid, adiabatic flow. Shading denotes the cold pool, contours show ψ (contour interval 0.05), and flow vectors are shown every fourth grid point. The dashed line indicates a 60° angle from the horizontal.

whether the gradient in ψ is larger in the vertical or horizontal direction). The distribution of $\eta(x, z)$ is adjusted accordingly. The iteration stops when errors in ψ and E do not exceed the threshold value anywhere along the interface, which is then held fixed for step 2.

Step 2 determines the shape of the interface between regions I and III. For $z < H$ the horizontal position of the boundary has some value at every height $x_s(z)$, which is originally assumed to be zero everywhere. Baroclinic vorticity on the interface is determined at each step of the iteration as follows:

$$\eta(x_s, z) = \begin{cases} -\sqrt{2\hat{b}s}/\Delta & \text{for } 0 \leq z \leq H \\ -\sqrt{2\hat{b}S}/\Delta & \text{for } H \leq z \leq d \end{cases}, \quad (26)$$

where $s(z)$ is the length of the interface from the surface to height z , and S is the total length from the surface to height H . We determine $s(z)$ numerically based on the shape of the interface $x_s(z)$. Along the interface, u is given by $u(x_s, z) = w dx_s/dz$ (i.e., the interface is assumed impermeable) and pressure ϕ is set equal to the hydrostatic pressure far behind the interface [(17)], the latter assumption being consistent with zero flow in the cold pool. The position of the interface at each height is then perturbed by a small amount left or right (depending on the sign of the error in E along the interface). The iteration stops once the error in E falls below some threshold value at all heights $0 < z < H$. A curvilinear grid that conforms to the interface x_s on the left boundary is used in this step so that interpolation is not required.

We use an analysis grid with 513×513 points over $0 \leq x/H \leq 6$ and $0 \leq z/H \leq 6$. The solution is shown in Fig. 2, focusing on the lower-left corner of the analysis grid near the cold-pool interface. The cold-pool interface is slightly concave, but is predominantly vertical. Near the surface the interface has a negative slope ($dx_s/dz < 0$), while for $z/H \geq 0.3$ it has a positive slope. The dashed line on Fig. 2 denotes a 60° angle from the horizontal at the surface, indicating the expected result at $z = 0$ (e.g., Rottman et al. 1985; Xu 1992).

This numerical solution demonstrates that the hypothesized optimal state satisfies the steady, inviscid, adiabatic equations of motion everywhere, although here we find that the interface is nearly (but not strictly) vertical. The key differences with past studies (e.g., Xu 1992) are that 1) we assume that the environmental flow follows the cold-air boundary up to a point of separation at $z = H$; and 2) we do not assume a horizontal rigid upper boundary on the analysis grid.

g. Flow separation for steady inviscid flow

From a general fluid dynamical point of view, flow separation in the inviscid limit is a delicate topic (e.g., Saffman 1992, his section 6.6). If we imagine for the moment the upper-right edge of the cold pool as a solid body, one can hypothesize either no separation (i.e., the flow goes left with an infinite acceleration as the flow rounds the corner point) or separation (with a discontinuous velocity field as pictured in Fig. 2). Saffman (1992, p. 108) makes the point (and we agree) that within the context of purely inviscid theory there is no way to choose between them.

A similar argument can be made with respect to buoyancy effects. At each point of the solution shown in Fig. 2, $\mathbf{u} \cdot \nabla b = 0$, since b is a constant in regions I–IV and, along the cold-air interface, ∇b is normal to \mathbf{u} for $0 < z \leq H$ (and $\nabla b = 0$ for $z > H$). In effect, the vorticity produced by the buoyancy gradient is within a sheet that lies between the cold air and the warm air up to $z = H$ and then separates, extending vertically upward for $z > H$ [see (26)].

The impact of these idealizations on the overall flow structure envisioned in Figs. 1 and 2 (the optimal state) will be assessed in the following sections using numerical simulations with the Navier–Stokes equations including heat diffusion.

3. Time-dependent numerical simulations

a. The numerical model

We analyze two-dimensional (2D) numerical simulations in this study. The numerical model uses the compressible Boussinesq equations:

$$\frac{\partial u}{\partial t} = -u \frac{\partial u}{\partial x} - w \frac{\partial u}{\partial z} - \frac{\partial \phi}{\partial x} + \frac{\partial \tau_{11}}{\partial x} + \frac{\partial \tau_{13}}{\partial z}, \quad (27)$$

$$\frac{\partial w}{\partial t} = -u \frac{\partial w}{\partial x} - w \frac{\partial w}{\partial z} - \frac{\partial \phi}{\partial z} + g \frac{\theta'}{\theta_0} + \frac{\partial \tau_{13}}{\partial x} + \frac{\partial \tau_{33}}{\partial z}, \quad (28)$$

$$\frac{\partial \theta'}{\partial t} = -u \frac{\partial \theta'}{\partial x} - w \frac{\partial \theta'}{\partial z} - \frac{\partial \tau_{\theta 1}}{\partial x} - \frac{\partial \tau_{\theta 3}}{\partial z}, \quad (29)$$

$$\frac{\partial \phi}{\partial t} = -c_s^2 \left(\frac{\partial u}{\partial x} + \frac{\partial w}{\partial z} \right), \quad (30)$$

where c_s is the speed of sound (set to a constant 300 m s^{-1}). We conduct direct numerical simulations (DNS) with the viscous stress τ_{ij} and conductivity $\tau_{\theta i}$ terms calculated as follows:

$$\tau_{ij} = \frac{\mu}{\rho_0} \left(\frac{\partial u_i}{\partial x_j} + \frac{\partial u_j}{\partial x_i} \right), \quad (31)$$

$$\tau_{\theta i} = -\frac{\kappa}{\rho_0} \frac{\partial \theta}{\partial x_i}, \quad (32)$$

where μ is dynamic viscosity and κ is thermal conductivity, both assumed constant. Unless stated otherwise, the Reynolds number $\text{Re} \equiv \rho_0 U H / \mu$ and is set to 10^4 [U and H are scaling parameters for this topic (defined below)]. The Prandtl number $\text{Pr} \equiv \mu / \kappa = 1$.

The model is integrated using the Runge–Kutta method for compressible flows from Wicker and Skamarock (2002). Advection terms use the fifth-order scheme from their study, except advection for θ' uses a weighted essentially nonoscillatory (WENO) scheme (Shen and Zha 2010). All other gradients are calculated using second-order centered finite differences on a standard staggered C grid. Open boundary conditions, following Durran and Klemp (1983, p. 2345), are used for the lateral boundaries. Upper and lower boundaries are flat, rigid, and use free-slip boundary conditions.

The model grid has 1600×640 grid points, and the domain depth is $8H$ (i.e., 8 times the initial cold-pool depth). All simulations are integrated for 180 min. Model output is saved every 15 s. The simulations are intentionally integrated for a long time ($>60T$, where $T = H/U$ is the dynamical time scale) because a primary goal of these simulations is to determine whether a time-dependent simulation can develop and maintain the flow described in Fig. 1.

b. Initial conditions

We decided not to initialize the model with the exact flow shown in Fig. 1; specifically, we do not initialize with a vertically oriented jet extending to a great height.

Rather, we take the opportunity to evaluate whether the model can produce this feature given only the essential ingredients of the problem, those being a stagnant cold pool within a sheared low-level environment.

For the initial cold pool, we specify a rectangular block of relatively cold air over the left half of the domain, that is, for $x \leq 0$ where $x = 0$ corresponds to the midpoint of the domain (as in Fig. 1). This initial cold pool has depth H with constant potential temperature deficit $\Theta \equiv \Delta\theta$ (or, equivalently, constant buoyancy $\hat{b} = -g\Delta\theta/\theta_0$). For the initial flow, we specify a simple two-dimensional (2D) distribution of horizontal vorticity η as follows:

$$\eta(x, z) = \begin{cases} -\sqrt{2\hat{b}z}/\Delta x & \text{for } -6\Delta x \leq x < 0, \quad 0 \leq z \leq H, \\ \sqrt{2\hat{b}H}/h & \text{for } x > 0, \quad 0 \leq z \leq h, \end{cases} \quad (33)$$

with $\eta = 0$ everywhere else, where h is the initial depth of the shear layer and Δx is the grid spacing. The velocity scale $U \equiv \sqrt{2\hat{b}H}$ and, unless stated otherwise, we set $h = 0.75H$ based on the results of the flow-force balance analysis (section 2d). The value $6\Delta x$ in the first line of (33) is arbitrary but is chosen so that the initial strip of negative vorticity is well resolved by the model.

With θ and η thus specified, initial values of the model's other variables (u , w , and ϕ) are determined as follows. Velocities u and w are retrieved from (9); we assume $\psi = 0$ at the lower/upper boundaries and $\partial\psi/\partial x = 0$ at the left/right boundaries. Then ϕ is determined from the equation

$$\frac{\partial^2 \phi}{\partial x^2} + \frac{\partial^2 \phi}{\partial z^2} = \frac{\partial F^u}{\partial x} + \frac{\partial F^w}{\partial z}, \quad (34)$$

where F^u and F^w represent the right-hand sides of (27) and (28) (omitting the pressure gradient terms).

Initial nondimensional fields u/U , w/U , θ'/Θ , and $\eta/(Uh^{-1})$ are shown in Fig. 3. An essential difference from some previous idealized simulations of gravity currents in shear is the flow in the cold pool, which is essentially stagnant in our case (Fig. 3); in contrast, RKW and Weisman and Rotunno (2004) specified vertical wind shear throughout the entire horizontal extent of the domain, including the cold pool.

Most analyses below are presented nondimensionally, although for reference we note that our model is actually written with dimensional equations and we have chosen $U = 15 \text{ m s}^{-1}$ and $H = 2.5 \text{ km}$; it follows that $h = 1.9 \text{ km}$, $\Theta = -1.4 \text{ K}$, $\mu = 3.75 \text{ kg m}^{-1} \text{ s}^{-1}$, and $\Delta x = 31.25 \text{ m}$.

4. A simulation of the optimal state

a. Evolution of the model simulation

Early evolution of the model simulation is shown in Fig. 4. A notable ‘‘starting vortex’’ forms on the

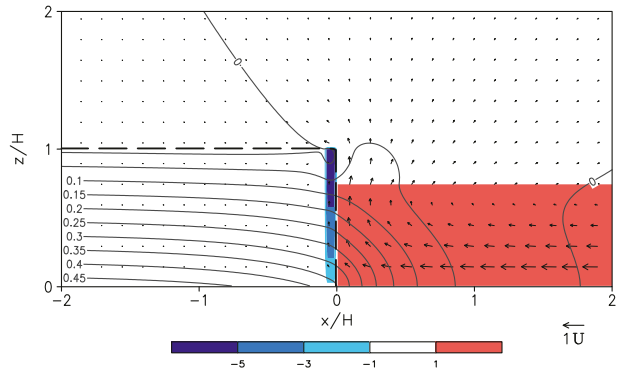


FIG. 3. Initial conditions near the edge of the cold pool. Color shading is horizontal vorticity $\eta/(Uh^{-1})$, the dashed black contour denotes the edge of the cold pool, and the gray contours show pressure $\phi/(UU)$ (contour interval 0.05). Flow vectors are shown every 12 grid points.

upper-right corner of the initial cold pool (Figs. 4a–b). This vortex grows upscale, consistent with the constrained two-dimensionality of this simulation, while moving upward and detaching from the surface-based cold pool (Figs. 4c–d). Later the starting vortex moves well away from the cold pool (Figs. 4e–f) and eventually interacts with the upper boundary (which is located at $z/H = 8$) (not shown). During this time, several smaller-scale vortices form near the upper-right corner of the cold pool; these vortices also detach from the cold pool and move upward. Flow behind the cold pool ($x/H < 0$) remains essentially zero throughout this time, except for very localized and transient areas near the vortices.

The second hour of the simulation is summarized in Figs. 5a–e. The overall structure and evolution remains the same throughout this period: that is, small-scale eddies form near the upper-right corner of the cold pool, detach from the cold pool, and move upward. Some complex vortex–vortex interactions sometimes occur above the cold pool, but the overall sense of the flow is essentially the same as depicted in the conceptual schematic (Fig. 1); that is, the sheared low-level environmental flow is turned into the vertical, resulting in a vertically oriented jet. This overall structure persists through the third hour of the simulation (e.g., Fig. 5f).

Time-averaged fields, calculated from output fields every 15 s, are shown in Fig. 6. For this analysis, the model output is shifted horizontally so that the position of the surface gust front is at a common location, $x_F = 0$; averaging in time is done after this normalization. The horizontal flow within the environment essentially ‘‘disappears’’ as it interacts with the cold pool (Fig. 6a). There is no notable time-mean horizontal flow anywhere else near the leading edge of the cold pool. The vertical flow (Fig. 6b) is highlighted by a vertically oriented jet with

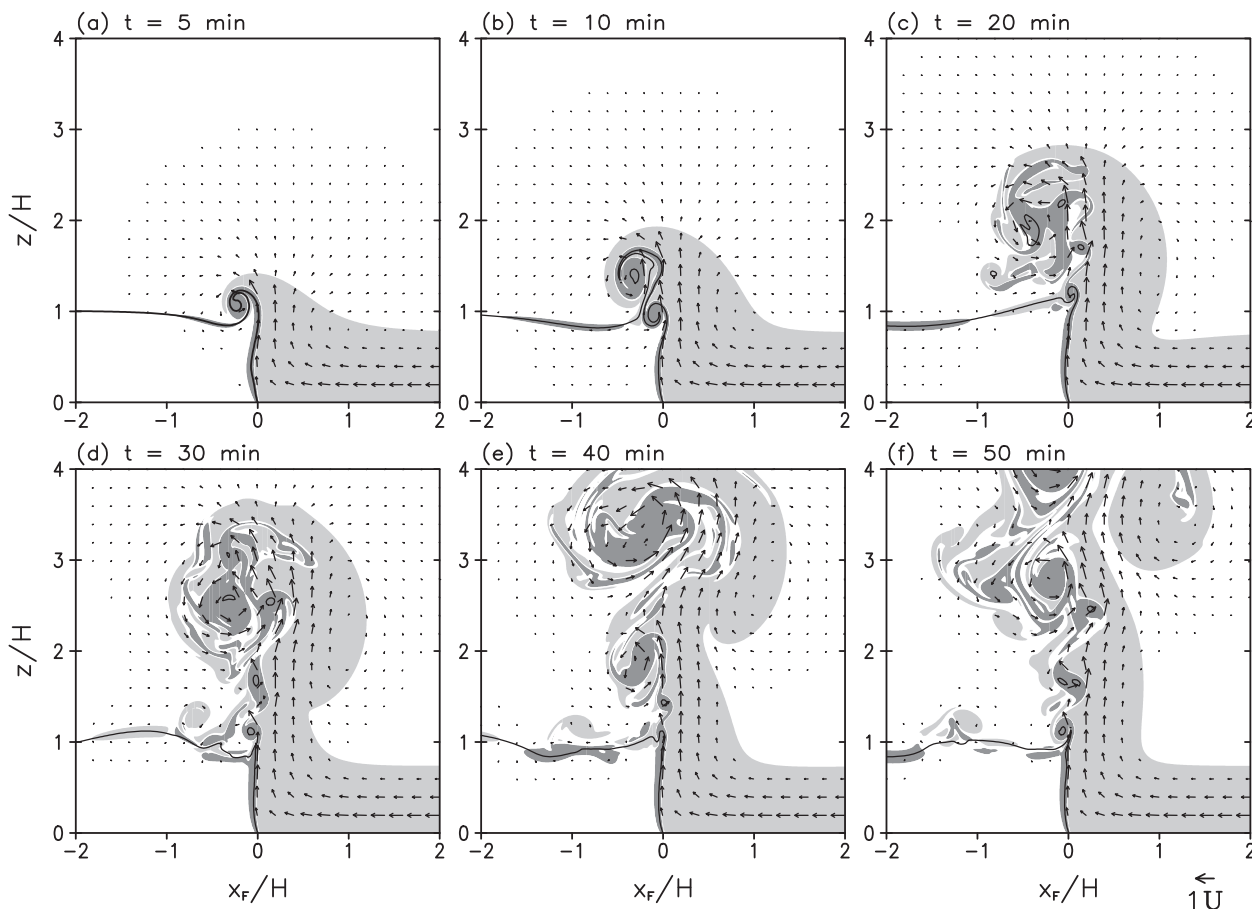


FIG. 4. Early evolution of the numerical simulation at $t =$ (a) 5, (b) 10, (c) 20, (d) 30, (e) 40, and (f) 50 min. Flow vectors are shown every sixteenth grid point; vectors with a magnitude less than $0.05U$ are excluded. The black contour shows $\hat{b} = 0.5$. Light shading denotes $\eta/(Uh^{-1}) > 0.5$, and dark shading denotes $\eta/(Uh^{-1}) < -0.5$.

a sharp horizontal gradient along the edge of the cold pool. At higher levels ($z/H > 1$) this gradient weakens, as does the maximum value of w in the jet, presumably because of mixing by the transient eddies. For $z/H > 2$, the average flow is downward above the cold pool (dashed contours in Fig. 6b), although this region is highly turbulent and w actually oscillates from positive to negative (not shown). The time-mean potential temperature field (Fig. 6c) shows that the cold pool remains roughly rectangular, with a nearly vertical leading edge above the surface gust front. (A closer examination of the structure is provided below.) A notable difference from the analytical models in section 2 is that some cold-pool air is drawn upward, along with baroclinically generated negative vorticity (Fig. 6d), from the upper-right corner of the cold pool. The viscous terms in the model and/or the resolved turbulence act to weaken the mean gradient of these variables as the fluid moves upward.

A closer look at the upper-right corner of the cold pool is shown in Fig. 7 with higher-frequency snapshots

(every 0.5 min). The environmental air is primarily directed upward at all times, as in the analytic models discussed in section 2 (hereafter referred to as the theoretical model). Also, flow to the left of the surface gust front ($x_F < 0$) is stagnant at all levels, also consistent with the theoretical model. The primary difference is the cold pool's corner point at $(x_F/H, z/H) \approx (0, 1)$; in the simulation there are transient turbulent eddies that continuously detach from the upper-right corner of the cold pool and move upward. These eddies carry negative values of θ' and η upward and roll up into discrete vortices because of the dominantly negative vorticity. The θ' contours eventually detach from the cold pool because of heat conductivity acting to weaken the gradient. In contrast, for the theoretical model we hypothesized a sharp corner to the cold air, with no upward transport of $\theta' < 0$. Despite the slightly different structure of the thermal field, the model simulation and the theoretical model have essentially the same overall features in the flow field near the cold-pool corner point, most notable

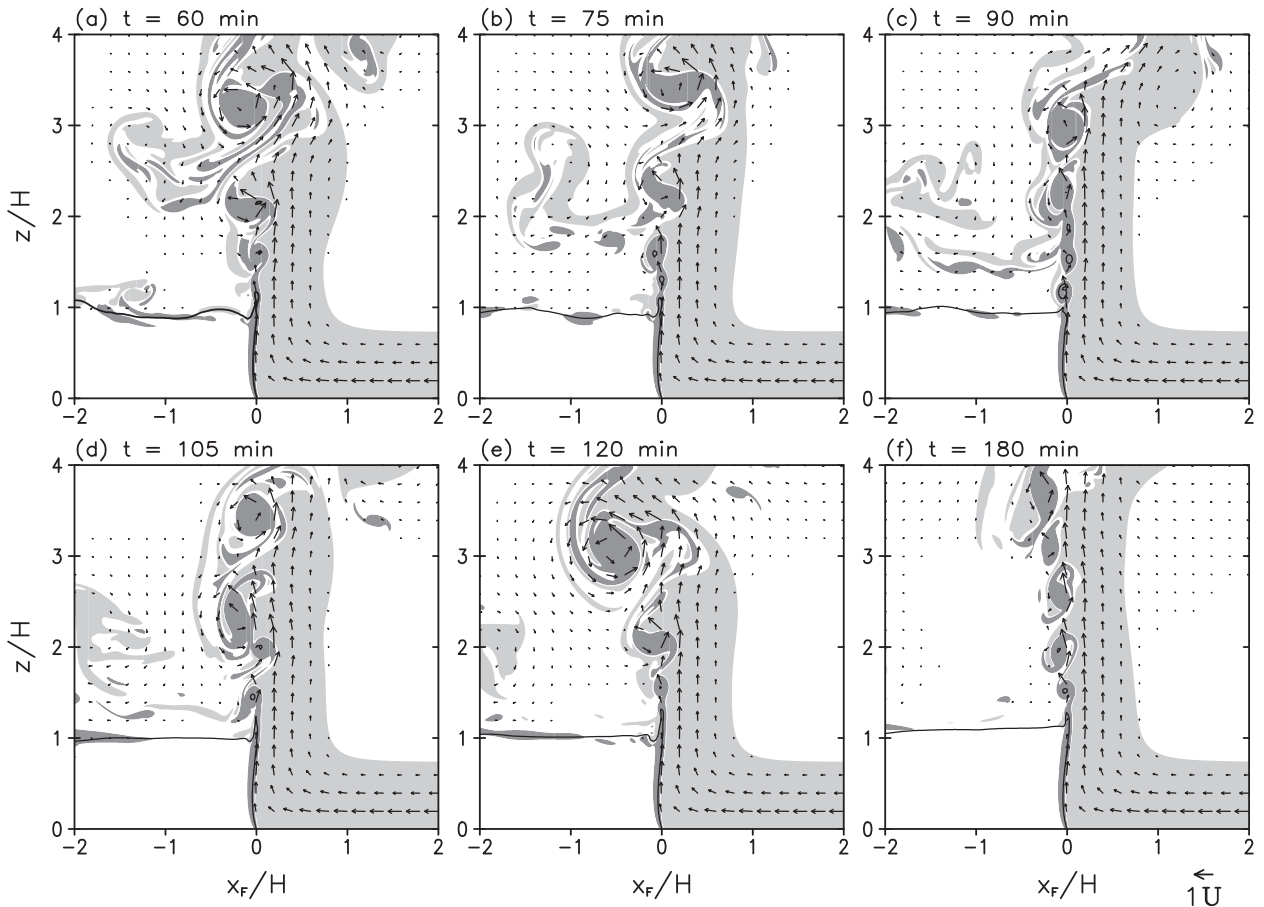


FIG. 5. As in Fig. 4, except showing later evolution of the numerical simulation at $t =$ (a) 60, (b) 75, (c) 90, (d) 105, (e) 120, and (f) 180 min.

being a sheet of negative vorticity on the left edge of the jet that extends upward from the upper-right corner of the cold pool (see also Fig. 6d).

We believe that the flow at the corner point shown in Figs. 4 and 5, and in greater detail in Fig. 7, is analogous to flow separation past a “salient edge” (i.e., sharp edge) of a rigid surface (e.g., Batchelor 1967, 329–330, Fig. 5.10.5). In the present case, baroclinic production plays the role of the no-slip condition at a salient edge in generating a vorticity distribution characterized by an unstable vortex sheet leaving the corner point (or salient edge). The small amount of cold fluid transported upward from the corner point (which is a unique aspect of the present flow) is quickly diffused away (Fig. 6c) and seems to have no impact on the existence of the vertical jet (Fig. 6b) that occurs in the optimal state.

b. Vorticity budget

In this section we analyze the time evolution of the vorticity budget in a CV, which featured prominently in the original presentation of the optimal state by RKW,

but which has been questioned by some later studies (e.g., Xu and Moncrieff 1994; Davies-Jones and Markowski 2013). Specifically, we analyze the budget expressed as follows:

$$\begin{aligned}
 0 = & \underbrace{-\frac{\partial}{\partial t} \int_L^R \int_0^d \eta \, dx \, dz}_{\text{tendency}} + \underbrace{\int_0^d (u\eta)_L \, dz}_{\text{flux at left}} - \underbrace{\int_0^d (u\eta)_R \, dz}_{\text{flux at right}} \\
 & - \underbrace{\int_L^R (w\eta)_d \, dz}_{\text{flux at top}} + \underbrace{\int_0^d (B_L - B_R) \, dz}_{\text{net generation}},
 \end{aligned}
 \tag{35}$$

where the analysis is conducted over a CV as described in Fig. 1. To be clear, the balance of terms for the optimal state was expressed by RKW as follows: “the import of the positive vorticity associated with the low-level shear just balances the net buoyant generation of negative vorticity by the cold pool in the volume” (p. 478); in

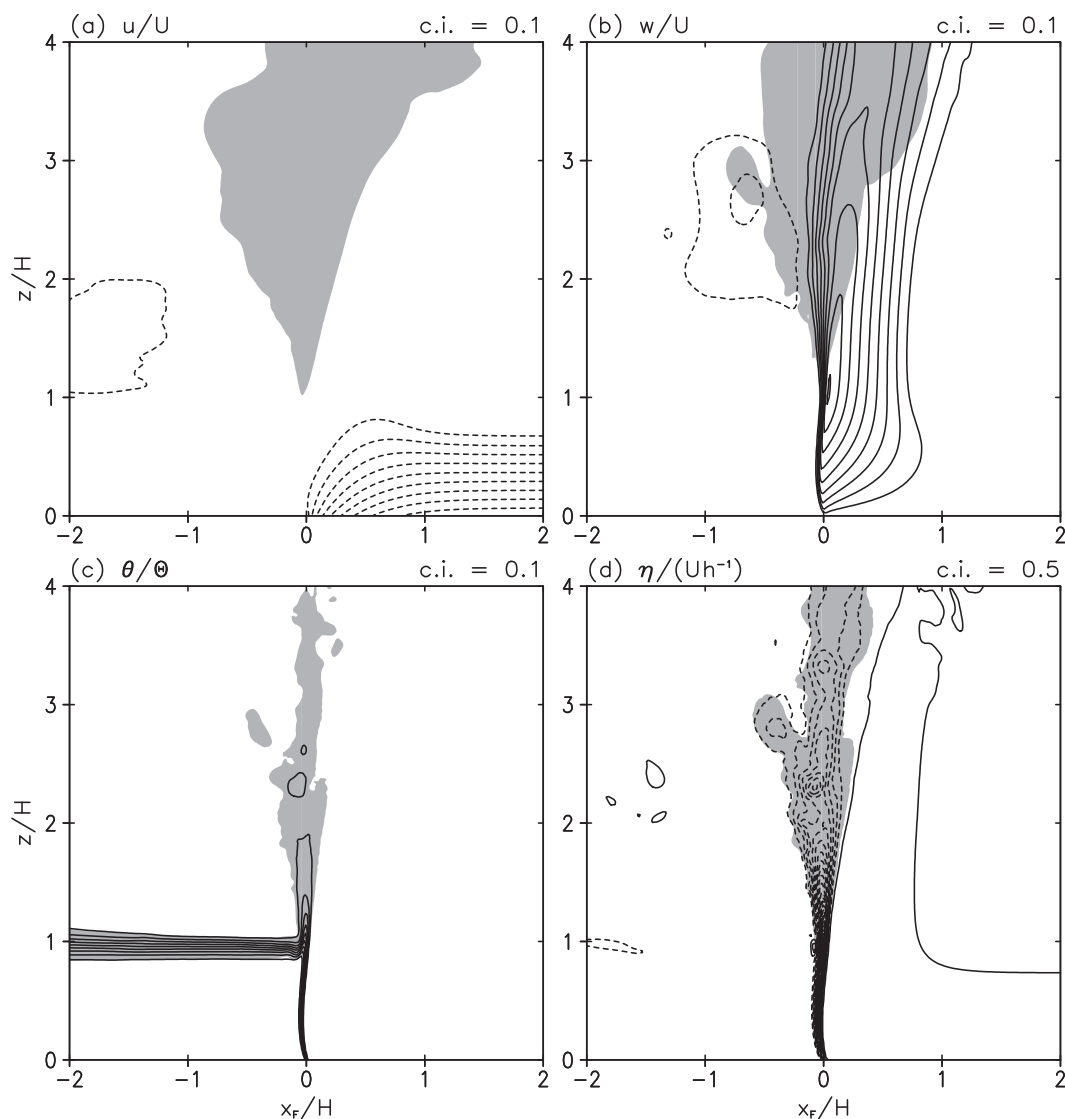


FIG. 6. Time-averaged variables (contours) and their variance (shading) for $t = 60$ – 120 min: (a) u/U (contour interval 0.1), (b) w/U (contour interval 0.1), (c) θ/Θ (contour interval 0.1), and (d) $\eta/(Uh^{-1})$ (contour interval 0.5). Dashed contours denote negative values, and the zero contour is excluded in all panels. Gray shading denotes variance (in time) greater than one-tenth of the maximum variance.

other words, the “flux at right” term balances the “net generation” term in (35).

A time series of each term in (35) from 60 to 120 min (i.e., $t/T = 21.6$ – 43.2) is shown in Fig. 8. The CV for this analysis is $-2 \leq x_F/H \leq 2$ and $0 \leq z/H \leq 2$. (Results are insensitive to changes in the size of the control volume as long as the left side is located at $x_F \lesssim -0.5$, the right side is located at $x_F \gtrsim 1$, and the top is in the range $1.5 \leq z/H \leq 6.5$.) The CV is centered on the surface gust front (located at $x = x_F$) and the mean translation of the control volume (which is small, $\approx 0.02U$) is subtracted from u for this analysis.

First, we consider terms that change negligibly throughout this time. The “flux at left” term (green line in Fig. 8) is clearly negligible compared to all other terms. Obviously this term is small because there is negligible development of horizontal flow behind the surface gust front (Figs. 4–7). This statement is valid at all levels; that is, this conclusion does not depend on the choice for d (the top of the CV). In a recent study of the topic, Davies-Jones and Markowski (2013) seem to advocate this “flux at left” term as a leading term in the vorticity budget (see page 1209 therein), but it is clearly negligible in this case.

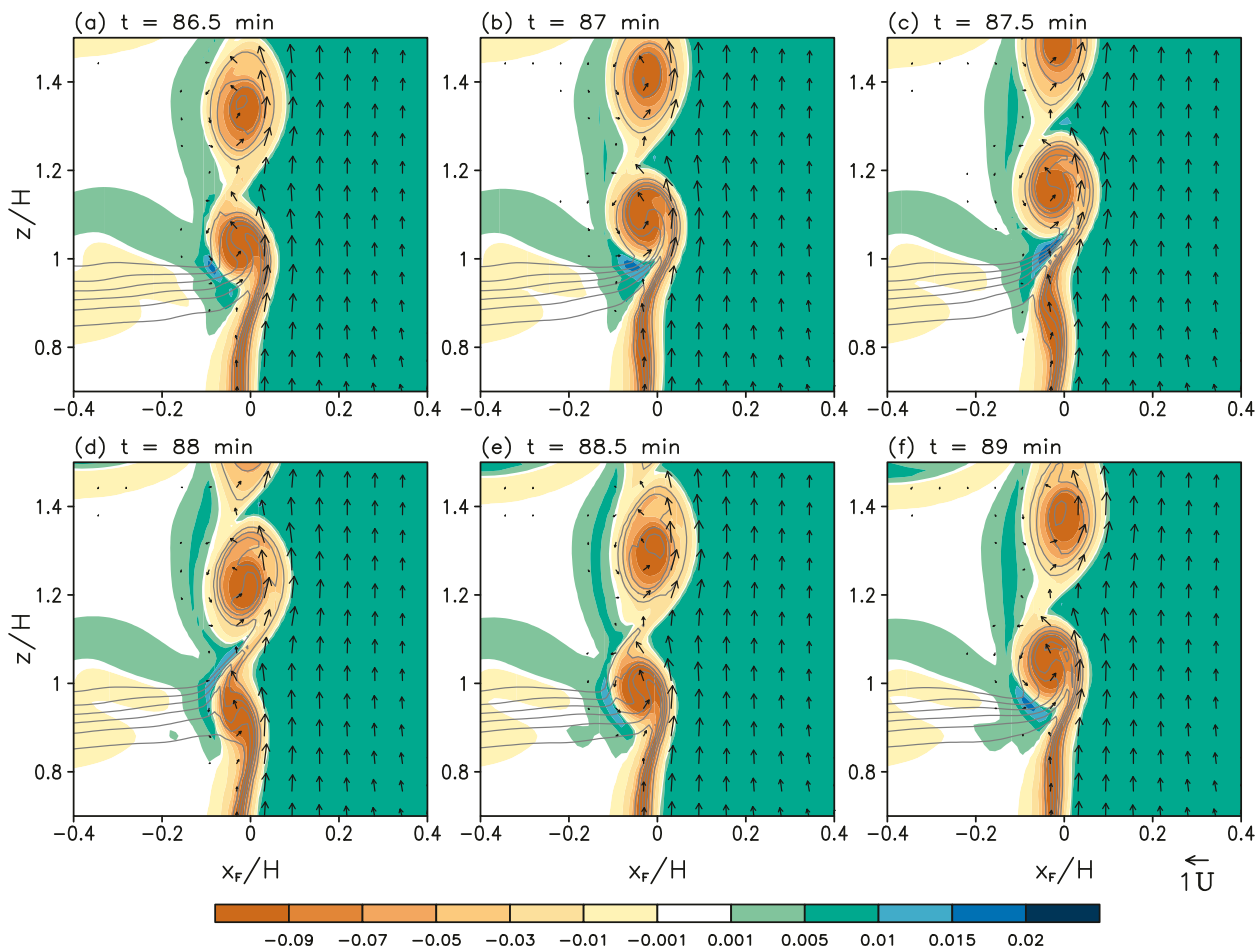


FIG. 7. Vorticity η (s^{-1} , color shading), flow vectors (every fifth grid point), and potential temperature θ (contours, every 0.2 K) near the upper-right corner of the cold pool plotted every 0.5 min from 86.5 to 89 min. Vectors with a magnitude less than $0.05U$ are excluded.

The largest terms (on average) in the vorticity budget are actually the “flux at right” term (red in Fig. 8) and the “net generation” term (blue in Fig. 8), consistent with RKW’s assessment (see above). In this simulation, the time-average values of these two terms are essentially equal in magnitude and opposite in sign (see top of Fig. 8).

The remaining terms from (35), which are shown on the right side of Fig. 8, were considered zero by RKW. In fact, the “flux at top” term (cyan line in Fig. 8) is technically not zero most of the time, consistent with a major conclusion by Davies-Jones and Markowski (2013). However, the occasionally large instantaneous values of the “flux at top” term are approximately canceled at all times by the “tendency” term (magenta term in Fig. 8). The time-averaged values of both terms are negligibly small compared to the leading terms in the budget (i.e., those discussed in the previous paragraph). The large-amplitude oscillations in the “flux at top” and “tendency”

terms occur because of the instability of the left side of the vertically oriented jet and the resulting transient turbulent eddies, which periodically pass through the upper boundary of the CV; because of their complex structure, sometimes these eddies transport vorticity through the top of the CV, and thus there is a rapid change of total vorticity in the CV. The eddies themselves are likely inevitable in numerical simulations of the optimal state, considering the highly sheared structure of the jet on its cold-pool side (i.e., left side). Consequently, a vorticity budget analysis based on one instantaneous snapshot of a simulation could be misleading, because the flow will not be strictly steady (in the sense that the time tendency term is not exactly zero). Nevertheless, the flow can be considered statistically steady (e.g., Wyngaard 2010) because the time-averaged tendency term is negligible.

The black line in Fig. 8 is the residual after adding all the other terms and represents the unexplained part

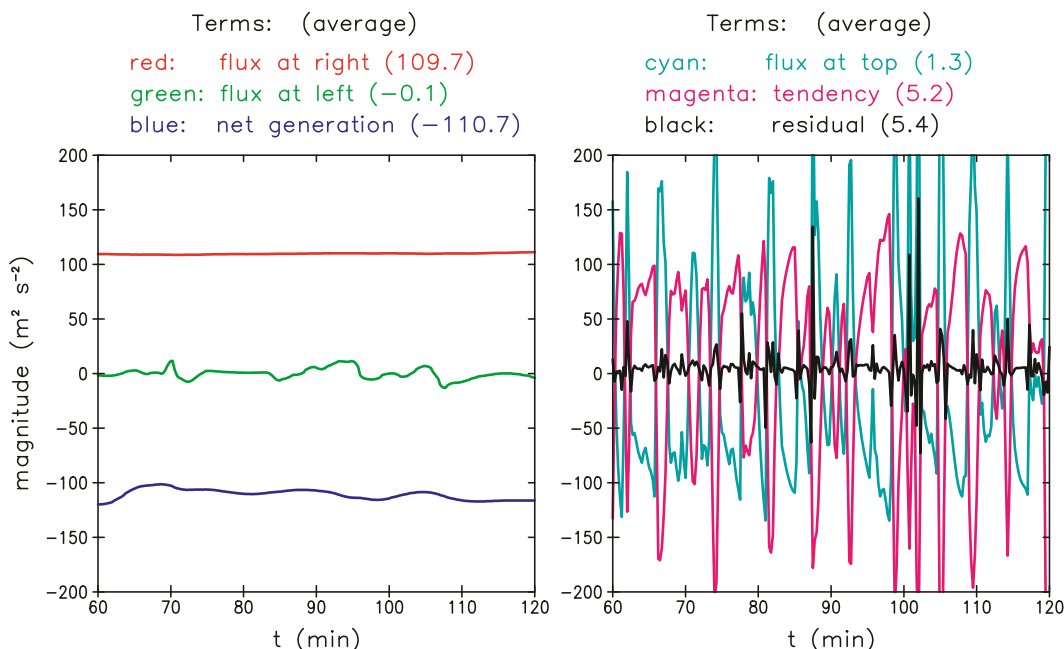


FIG. 8. Time evolution of terms in the horizontal vorticity budget, as indicated by the legend at the top [corresponding to terms in (35)]. Numbers in parentheses in the legend denote the average value over this time period. The control volume for this analysis is $-2 \leq x_F/H \leq +2$ and $0 \leq z/H \leq 2$.

of the vorticity budget. This term is negligibly small throughout the simulation and presumably represents the viscous terms that have not been considered here.

c. Flow associated with vorticity

The basic premise of RKW's theory (section 2b) is that two processes can oppose each other, those being flow associated with negative vorticity at the edge of the cold pool, and flow associated with positive vorticity in the environment. The primary purpose of the vorticity budget analysis by RKW was to obtain a quantitative criterion for when these processes are exactly balanced. To illustrate these effects, in Fig. 9a we show the total vorticity and actual flow vectors from an instantaneous snapshot of our simulation. In Fig. 9b we show only the positive vorticity and the flow associated with that particular distribution of vorticity, which we determine from (9) (using only the positive vorticity for the right-hand side, with vorticity elsewhere set to zero). In Fig. 9c we show only the negative vorticity and the flow associated with that particular distribution of vorticity from (9) (using only the negative vorticity for the right-hand side). The sum of the flow from Figs. 9b and 9c is practically identical to the actual flow from the model simulation; the maximum error is approximately $0.001U$.

The most notable feature of Fig. 9 is that the stagnant flow in the cold pool arises from a cancellation of flow

induced by environmental vorticity (which, by itself, would accelerate cold air to the left; Fig. 9b) and flow induced by the baroclinically generated vorticity (which, by itself, would accelerate cold air to the right). A similar conclusion is drawn for flow just above the cold pool (i.e., for $1 < z/H < 2$ and $x_F < 0$); also, in this region, the tendency for the flow to sink because of the nearby negative vorticity of the cold pool is countered by the tendency for the flow to rise because of the nearby positive vorticity of the environment.

From Fig. 9, we also note that the negative vorticity field is confined to a small area but has relatively large amplitude. In comparison, the positive vorticity is much smaller in amplitude (by an order of magnitude) but is much broader in extent. We point out these features to clarify that the magnitudes of positive and negative vorticity fields can be very different in the optimal state.

d. Pressure field

To provide another perspective, we examine the perturbation pressure field ϕ from the model near the leading edge of the cold pool (contours in Fig. 10a). Vectors in this figure illustrate acceleration \mathbf{F} associated with pressure and buoyancy; that is, $\mathbf{F} = (-\partial\phi/\partial x, -\partial\phi/\partial z + B)$. The primary feature of interest is the triangular-shaped region of relatively high perturbation pressure ahead of the cold pool ($x_F > 0$) near the surface (Fig. 10a). This

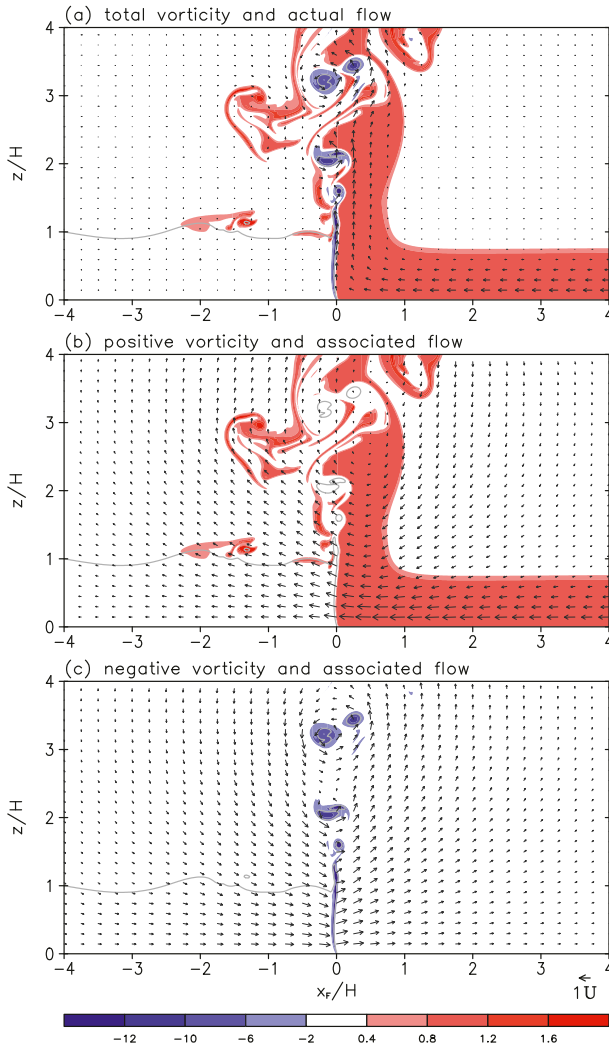


FIG. 9. (a) Actual vorticity $\eta/(Uh^{-1})$ (color shading) and actual flow vectors from the simulation at $t = 120$ min. (b) Positive vorticity and associated flow from (9). (c) Negative vorticity and associated flow from (9). The gray contour denotes $\hat{b} = 0.5$.

“bubble high” acts to decelerate the oncoming environmental flow and to accelerate flow in the vertical direction. Above the cold pool, there is a region of relatively low pressure that is collocated with the negative vorticity along the (left) side of the vertically oriented jet (Fig. 6d).

An especially noteworthy feature of Fig. 10a is that significant vertical acceleration is upward everywhere; in other words, there is no significant downward acceleration anywhere in Fig. 10a. This situation is consistent with a key element of RKW’s optimal state concept, in which vertical displacements are not “inhibited” by either the cold pool or the shear (RKW, p. 481).

For further insight, we decompose the pressure field into components associated with buoyancy ϕ_B and dynamics ϕ_D following several other studies in the severe

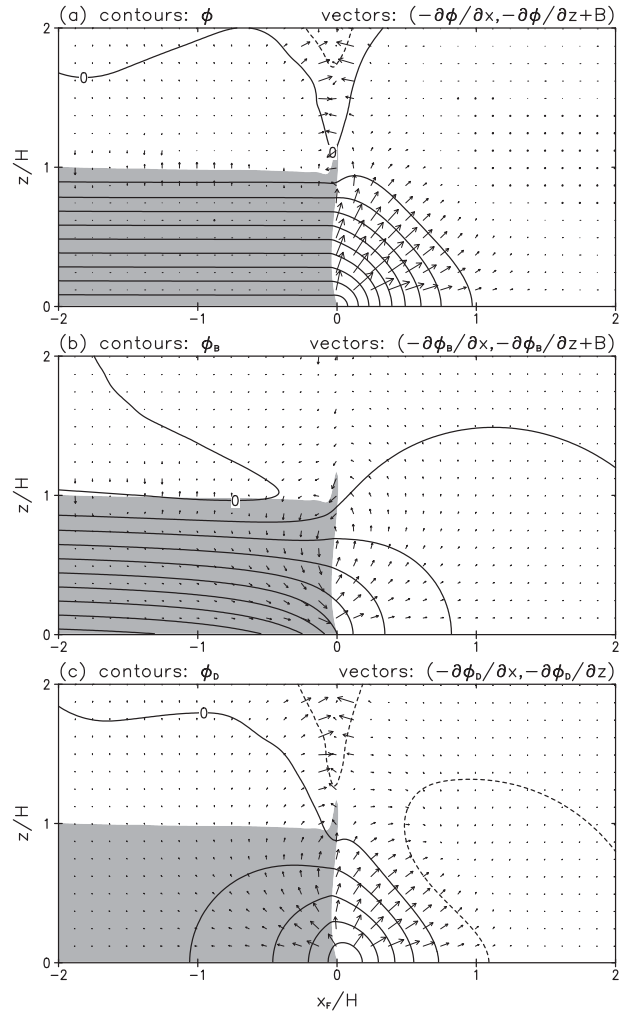


FIG. 10. Perturbation pressure (contours) and associated acceleration (vectors) using (a) actual pressure from the numerical model ϕ . (b) “buoyancy pressure” ϕ_B [determined from (36)], and (c) “dynamic pressure” ϕ_D [determined from (37)]. The contour interval in all panels is 0.05 (nondimensional units). For (a) and (b), buoyancy B is included in the vertical acceleration vectors. All fields are averaged from 60 to 120 min.

storms literature (e.g., Rotunno and Klemp 1985; Trapp and Weisman 2003). The relevant equations for our numerical model (which makes the Boussinesq approximation, and considers reference density to be constant) are as follows:

$$\nabla^2 \phi_B = \partial B / \partial z, \tag{36}$$

$$\nabla^2 \phi_D = -\nabla \cdot (\mathbf{u} \cdot \nabla \mathbf{u}). \tag{37}$$

The variables ϕ_B and ϕ_D are shown by contours in Figs. 10b and 10c, along with vectors illustrating the associated acceleration, \mathbf{F}_B and \mathbf{F}_D , as noted by captions on each figure panel. Both ϕ_B and ϕ_D contribute roughly

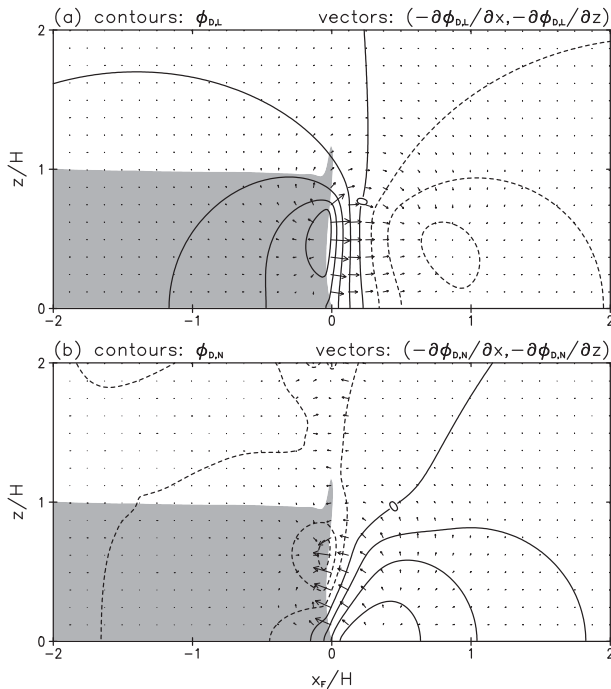


FIG. 11. As in Fig. 10, but for (a) linear dynamic pressure $\phi_{D,L}$ [determined from (38)] and (b) nonlinear dynamic pressure $\phi_{D,N}$ [determined by $\phi_{D,N} = \phi_{D,L} - \phi_D$].

equally to the maximum amplitude of the bubble high, although gradients in ϕ_D are larger and thus contribute to larger accelerations ahead of the gust front. Interestingly, just behind the surface gust front, this analysis shows that the downward tendency attributable to buoyancy (vectors in Fig. 10b) is exactly offset by an upward tendency attributable to ϕ_D (vectors in Fig. 10c), leading to zero net acceleration within the cold pool (Fig. 10a). Above the cold pool, the region of relatively low pressure is attributable entirely to ϕ_D .

We further decompose ϕ_D into a linear component, determined by

$$\nabla^2 \phi_{D,L} = -2 \frac{du_0}{dz} \frac{\partial w}{\partial x} \quad (38)$$

(e.g., Rotunno and Klemp 1982), where $u_0(z)$ is the ambient environmental wind profile. Nonlinear dynamic pressure is then determined simply by $\phi_{D,N} = \phi_D - \phi_{D,L}$. This decomposition, shown in Fig. 11, shows that the deceleration of the environmental flow is accomplished primarily by $\phi_{D,L}$ (Fig. 11a). To clarify, this analysis of $\phi_{D,L}$ shows the well-known “updraft in shear” effect, in which updrafts in a sheared environment are accelerated in the downshear direction. The nonlinear dynamic pressure, shown in Fig. 11b, is more difficult to interpret because it involves several flow effects (e.g., Rotunno and

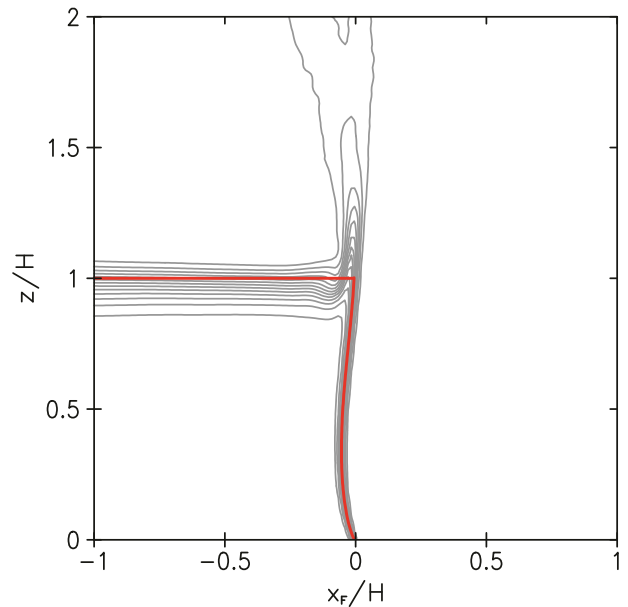


FIG. 12. Comparison of the theoretical interface for steady, inviscid, isentropic flow (red) with time-averaged (90–120 min) potential temperature from the numerical simulation (gray contours).

Klemp 1982), although we note that $\phi_{D,N}$ is the largest contributor to lifting ahead of the cold pool, and that the low pressure area above the cold pool is attributable to $\phi_{D,N}$.

e. Shape of the interface

The theoretical shape of the interface for steady, inviscid, isentropic flow that was determined in section 2f is compared with model output in Fig. 12, where the gray contours show time-averaged (90–120 min) potential temperature. The similarity is striking for $z/H < 1$ (i.e., below the nominal top of the cold pool) and adds confidence to conclusions drawn in sections 2e–g. Of course, the primary difference is the negatively buoyant air that is drawn upward in the model simulation, which is not considered in the theoretical solution. We reiterate the conclusion that a gravity current interface can be nearly, although not strictly, vertical in the presence of sufficient low-level shear (i.e., $\Delta u = \sqrt{2\hat{b}H}$ for any wind profile) that is distributed in a certain way (i.e., with $h/H = 3/4$ for a linear wind profile; further wind profiles are considered in section 6).

5. Additional simulations

a. Effects of viscosity

In the optimal-state simulation (section 4), transient turbulent eddies develop continuously along the leading

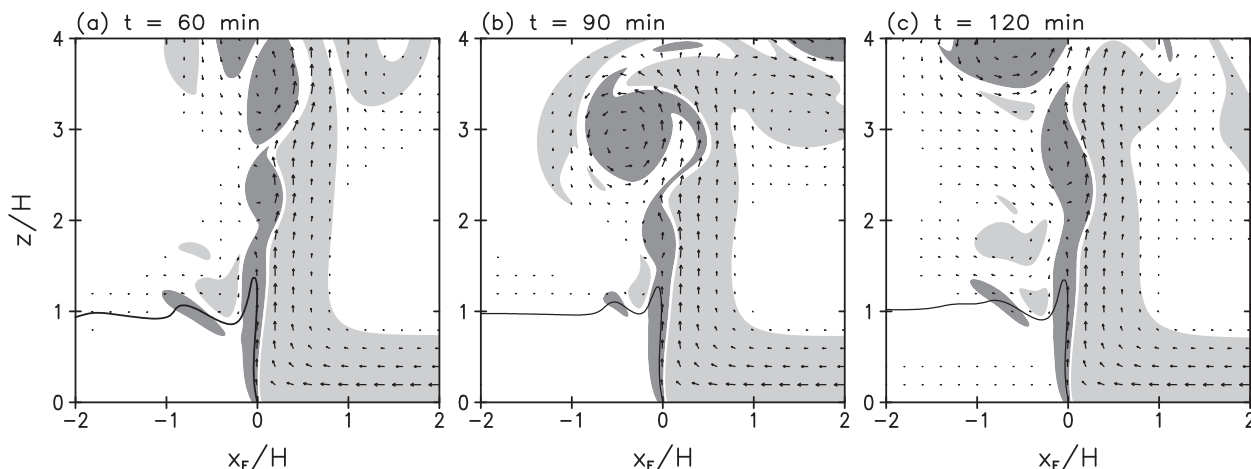


FIG. 13. As in Fig. 4, but from a simulation with lower $Re (=10^3)$ at $t =$ (a) 60, (b) 90, and (c) 120 min.

edge of the cold pool and move upward, detaching from the main body of cold pool (e.g., Figs. 4 and 5). The properties of these transient eddies are affected by changes in Re in our numerical model. We show a simulation with an order-of-magnitude lower value, $Re = 10^3$, in Fig. 13. (There are no other changes from the “control” simulation.) In general, the transient eddies tend to be larger in size and slower to evolve as Re decreases (i.e., as μ increases). Nevertheless, the overall structure of the optimal state—wherein the environmental flow is turned into a vertically oriented jet, with stagnant flow (relative to the surface gust front) everywhere behind

the gust front—is still produced by the model. Consistent conclusions are drawn from simulations in which the Reynolds number is increased compared to the control value (not shown).

The evolution of the vorticity budget [(35)] for the low- Re simulation is shown in Fig. 14. As in the control simulation, the most important terms in the vorticity budget are the “flux at right” and “net generation” terms, which are opposite in sign and roughly equal in magnitude. The primary difference from Fig. 8 occurs with the “flux at top” and “tendency” terms; consistent with weaker and more slowly evolving eddies, these terms are

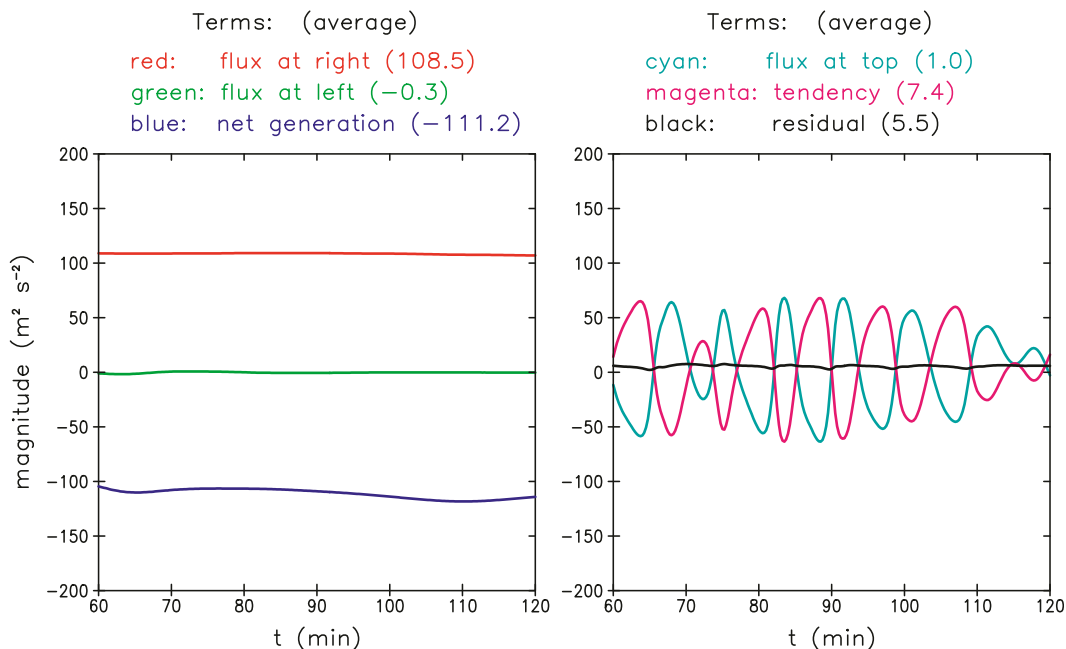


FIG. 14. As in Fig. 8, but from a simulation with lower $Re (=10^3)$.

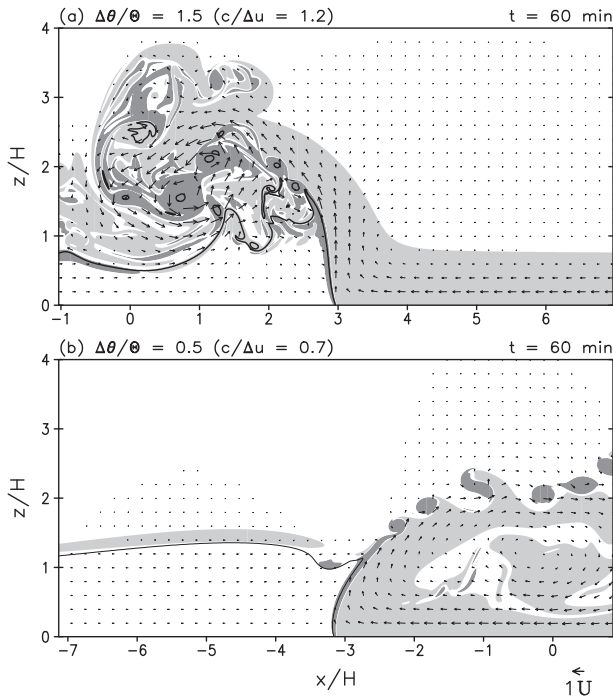


FIG. 15. As in Fig. 4, but at $t = 60$ min for (a) a simulation initialized with a stronger cold pool ($\Delta\theta/\Theta = 1.5$; $c/\Delta u = 1.2$) and (b) a simulation initialized with a weaker cold pool ($\Delta\theta/\Theta = 0.5$; $c/\Delta u = 0.7$).

lower in magnitude, and oscillate with a much longer period, compared to the control simulation.

b. Simulations with nonoptimal conditions

An important conclusion from section 2 is that the optimal state arises only when a set of dynamical constraints are met. That is, the magnitude of cold-pool intensity $c \equiv \sqrt{2b}H$ must match the change in horizontal velocity Δu across a linear wind profile in the environment [see (14)] and the depth of this shear layer must be $3/4 H$ [see (19)]. To be clear, these constraints are not required for there to be a (steady) cold pool in a sheared environment, nor are they required for deep lifting of environmental air (where “deep lifting” means vertical displacements greater than the depth of the cold pool H). Rather, these constraints are required for the flow depicted in Fig. 1 to be realized, which RKW argued leads to maximum possible (i.e., optimized) lifting of environmental air. So, as a demonstration of what happens when the constraints from section 2 are not met, we show here simulations in which the initial conditions are changed in subtle ways. All model settings and initial conditions are otherwise identical to the control simulation evaluated in section 4. We show that the basic premise of RKW’s theory (see section 2b) concerning the relative roles of

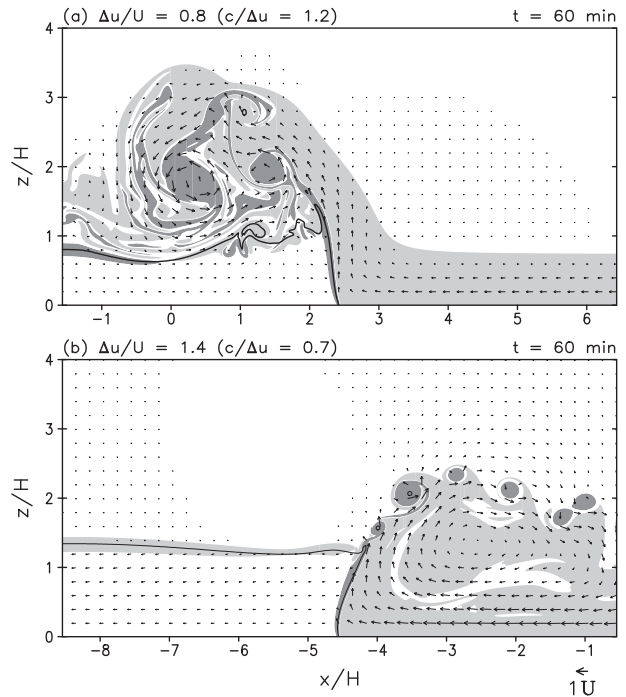


FIG. 16. As in Fig. 4, but at $t = 60$ min for (a) a simulation initialized with weaker environmental shear ($\Delta u/U = 0.8$; $c/\Delta u = 1.2$) and (b) a simulation initialized with stronger environmental shear ($\Delta u/U = 1.4$; $c/\Delta u = 0.7$).

the cold pool and shear are still valid even if these two effects are not balanced.

For Fig. 15 the initial potential-temperature difference $\Delta\theta$ across the cold pool is either increased by 50% (Fig. 15a) or decreased by 50% (Fig. 15b). [The initial wind fields $u(x, z)$ and $w(x, z)$ are identical to the control simulation.] After 1 h, in the simulation with a stronger cold pool (Fig. 15a) the environmental air is swept over the top of the cold pool. In contrast, in the simulation with a weaker cold pool (Fig. 15b) environmental air overturns and moves generally in the downshear direction (although some air sinks and “recirculates” back toward the gust front). For both of these simulations, there is negligible transport of low-level air into the upper half of the model domain (i.e., $z/H > 4$). The results of both simulations are consistent with RKW’s basic theory; that is, the trajectory of environmental air (relative to the surface gust front) depends on the relative intensity of the cold pool and the shear: when cold-pool effects are stronger than shear effects ($c/\Delta u > 1$, Fig. 15a) environmental air is swept over the cold pool, and when cold-pool effects are weaker than shear effects ($c/\Delta u < 1$, Fig. 15b) environmental air is swept downshear.

The same overall conclusions are drawn from simulations in which initial cold-pool properties are identical

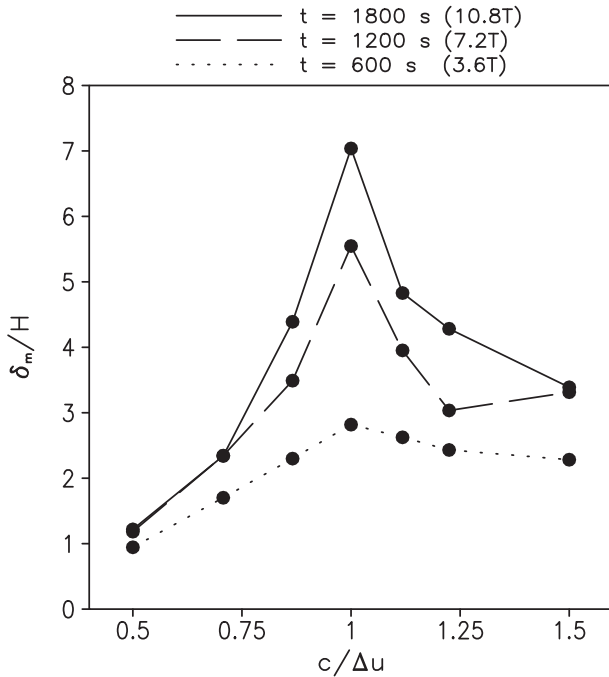


FIG. 17. Maximum nondimensional vertical displacements δ_m/H for fluid originating in low levels (initial height $z/H < 1$) after 600 (dotted), 1200 (dashed), and 1800s (solid).

to the control simulation but the magnitude of environmental shear is different. For the simulation shown in Fig. 16a the initial horizontal wind difference across the shear layer Δu is decreased by about 20%; the initial value of $c/\Delta u$ is 1.2 (as in Fig. 15a). Consistent with a cold-pool intensity that is stronger than the shear intensity, environmental air is swept over the top of the cold pool. For the simulation shown in Fig. 16b, the initial value of Δu is increased by about 40%; the initial value of $c/\Delta u$ is 0.7 (as in Fig. 15b). Consistent with theory, the environmental air is swept generally downshear.

c. Lifting of environmental air

Use of the term “optimal” by RKW refers specifically to lifting of environmental air by gravity currents in shear. In principle, the deepest lifting (i.e., the optimal state) occurs when a vertically oriented jet is created and maintained. Actually, in principle, lifting in the RKW optimal state is uninhibited, meaning that lifting can occur without limit. We evaluate this concept from numerical simulations as in Weisman and Rotunno (2004) by using a passive tracer $s(x, z, t)$ with initial condition $s(x, z, 0) = z$. The distribution of s at later times provides a quantitative measure of displacement by the value of $\delta = z - s$ at every grid point. We initialize s after 1 h of integration and analyze maximum displacements of low-level tracer $\delta_m = \max(z - s)$

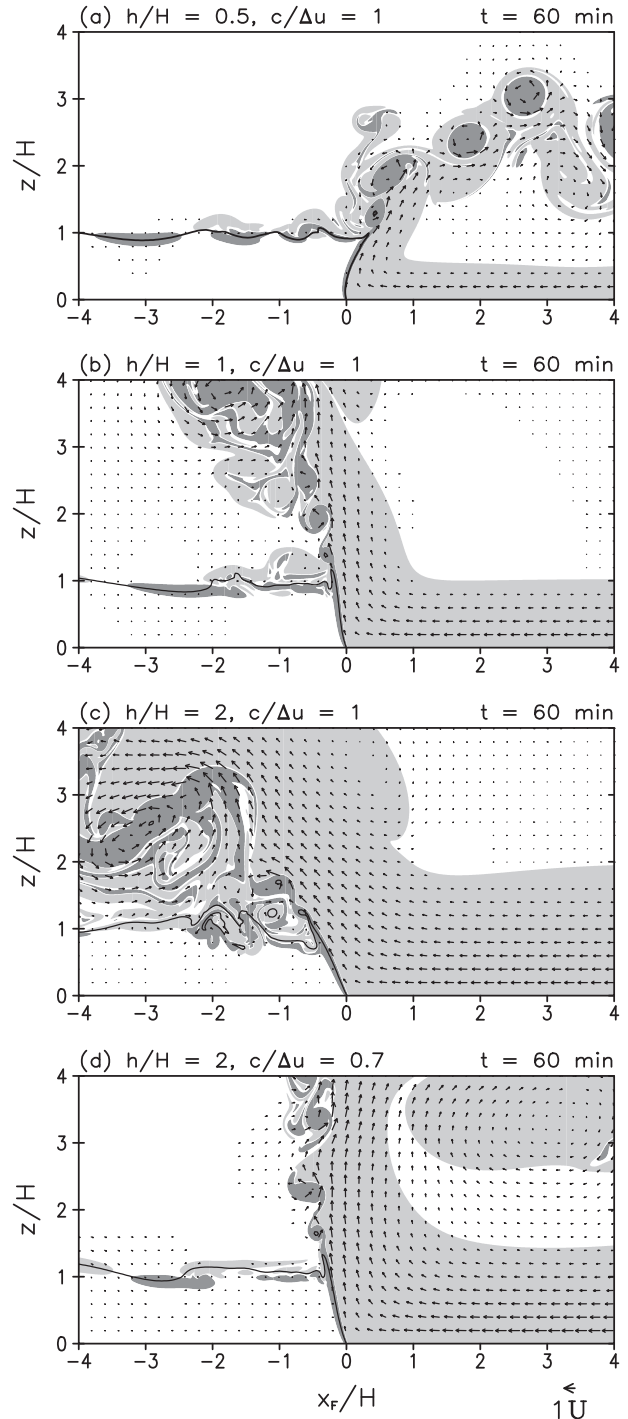


FIG. 18. As in Fig. 4, but at $t = 60$ min for simulations initialized with (a) $h/H = 0.5$, (b) $h/H = 1$, (c) $h/H = 2$, and (d) $h/H = 2$ with a 40% increase in Δu (such that $c/\Delta u = 0.7$).

(for $s \leq z/H$ only) at various times thereafter. Results are shown in Fig. 17 for the simulations with different initial cold-pool intensity (described in the previous subsection). Maximum displacement occurs with the

control simulation, that is, the simulation analyzed in section 4 for which $c/\Delta u = 1$, in which the vertically oriented jet is produced and maintained; this statement is valid for all times analyzed here, that is, after 600, 1200, and 1800 s (corresponding to nondimensional times $t/T = 3.6, 7.2,$ and 10.8). We note that the top of the model domain is $8H$, so essentially maximum possible lifting has been achieved in the control simulation at the final time analyzed here.

d. Depth of shear layer

In past studies on the optimal state for gravity currents in shear, it has been suggested that the depth of the environmental shear layer should be roughly equal to the depth of the cold pool, that is, $h/H \approx 1$ (e.g., RKW, p. 477; Weisman and Rotunno 2004, p. 371). In fact, a notable result from the flow-force balance analysis (section 2d) is that $h/H = 3/4$ is a requirement for the optimal state (assuming a linear wind profile). To evaluate this result, we have conducted simulations with different shear-layer depths compared to the nominal cold-pool depth. Results for shallower shear-layer depths (e.g., Fig. 18a) show an overall tilt of the updraft away from the cold pool with height. Another notable result is that the flow does not simply overturn and recirculate into the low-level environment, as in the simulations in which the ratio $c/\Delta u$ was modified (Figs. 15b and 16b); rather, the environmental air ascends to $z/H \approx 2.5$, which is notably higher than the initial shear-layer depth. For deeper initial shear-layer depths, the environmental air flows primarily over the cold pool (Figs. 18b,c). The “tilt” of the updraft away from the vertical increases as h/H increases. Overall, the simulations shown in Figs. 18a–c, along with the control simulation shown in Figs. 4 and 5, support a primary conclusion from the theoretical analysis in section 2, namely that more than one dynamical constraint is required for the optimal state to be realized.

For simulations in which the optimal state is not realized, the underlying dynamical arguments advanced by RKW (section 2b) are still valid. As an example, in Fig. 18d we show results from a simulation with $h/H = 2$ but with initial Δu increased by 40% compared to the control value. Comparing the two simulations in which everything is the same except Δu (Figs. 18c,d), the overall result is as expected; that is, the environmental flow is biased more toward the right (i.e., away from the cold pool) as the ratio of $c/\Delta u$ decreases.

6. Shear profile

Before concluding, we note that all preceding material in this article was based on the assumption of a linear

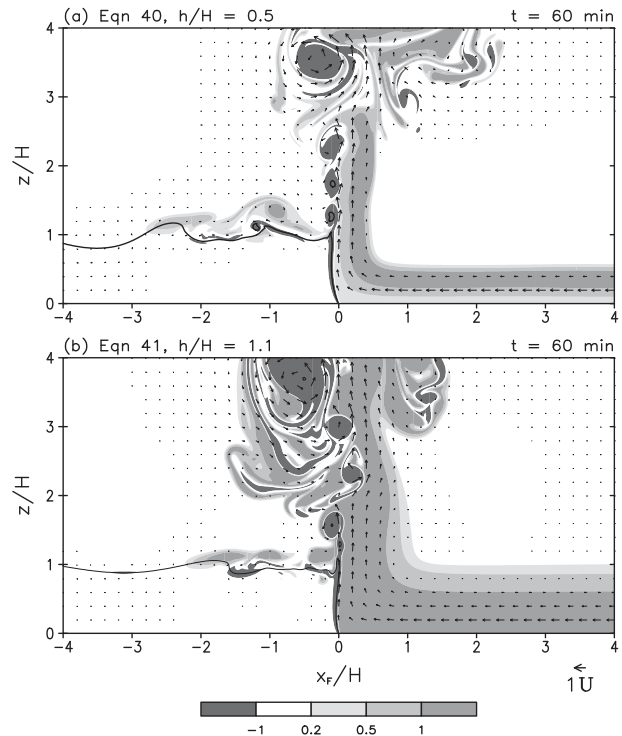


FIG. 19. As in Fig. 4, but at $t = 60$ min for (a) a simulation initialized with the wind profile (40) and $h/H = 0.5$, and (b) a simulation initialized with the wind profile (41) and $h/H = 1.1$. Shading denotes nondimensional vorticity $\eta/(Uh^{-1})$ as indicated by the color bar.

environmental wind profile [(11)]. This assumption is not required, and was made throughout this article primarily for simplicity. In this section we briefly note the consequences of assuming different shear profiles.

For the control volume analysis based on the vorticity equation (section 2c) the result [(14)] is not affected by a change in the structure of the shear profile. As long as flow at the top of the sheared layer is zero (i.e., flow in region IV is stagnant), and u at the bottom of the shear profile is U , then (14) remains the solution.

For the flow-force balance analysis (section 2d), the result is significantly different for different wind profiles because the form of $u(R, z)$ affects the vertically integrated horizontal momentum flux on the right side of the control volume [i.e., the first term in (16)], which must match the vertical integral of the hydrostatic pressure in the cold pool. For the linear wind profile [(11)], the final result of this analysis is the constraint $h/H = 3/4$. We now consider different wind profiles to illustrate how results can be different.

For a step function in velocity, in which environmental vorticity is confined to a sheet at $z = h$, the profile is given simply by

$$u(R, z) = \begin{cases} -U & \text{for } z \leq h \\ 0 & \text{for } z > h \end{cases} \quad (39)$$

Using (39) in (16), and performing the same steps as in section 2d, the solution is $h/H = 1/4$. In this case the inflow layer must be much shallower (by a factor of 3, compared to the case of the linear wind profile) for the optimal state to be realized. Testing this result with a numerical simulation is not feasible because the environmental vorticity is confined to a single grid point in the vertical, and is unstable to Kelvin–Helmholtz instability.

For the wind profile,

$$u(R, z) = -U \cos \frac{\pi z}{2h} \quad \text{for } z \leq h, \quad (40)$$

the environmental vorticity $\eta = \partial u / \partial z$ is a function of height, with largest vorticity near $z = H$ and zero vorticity at $z = 0$. In this case, the steps in section 2d yield the solution $h/H = 1/2$. In comparison, for the wind profile,

$$u(R, z) = U \left[\cos \frac{\pi}{2} \left(1 - \frac{z}{h} \right) - 1 \right] \quad \text{for } z \leq h, \quad (41)$$

the environmental vorticity is largest at $z = 0$ and decreases to zero at $z = h$. In this case, the steps in section 2d yield the solution $h/H = (6 - 16/\pi)^{-1} \approx 1.1$. These two wind profiles, with their associated constraints on h/H , were used in numerical model simulations, following the same procedure as the control simulation (section 3). Results (Fig. 19) show that the optimal state structure—a vertically oriented jet—is produced in the model.

In summary, a linear environmental wind profile is not a requirement for the optimal state, and the constraint on h/H is dependent on the profile of $u(z)$.

7. Summary and conclusions

This study presents a detailed examination of the theoretical “optimal state” for gravity currents in shear, which was first proposed by Rotunno et al. (1988, herein RKW). The optimal state is illustrated in Fig. 1 and the key feature is an environment with near-surface vertical wind shear that is turned into the vertical at the edge of a cold pool. The primary differences between this conceptual model and other theoretical models for gravity currents in shear (e.g., Xu 1992) are that 1) there is no rigid upper boundary and 2) there is separation of the environmental flow from the cold pool at some height H . The assumption of stagnant flow (relative to the surface gust front) in the cold pool is common in analytic studies of gravity currents (e.g., RKW; Xu 1992), although it is technically not necessary (e.g., Weisman 1992; Xu and

Moncrieff 1994); however, the ability to maintain stagnant flow at all levels on the left side is a significant feature of the RKW optimal-state model, because it highlights a fundamental difference from other gravity current models that assume (a priori) nonzero horizontal flow somewhere on the left side. Although the RKW optimal-state flow structure is not required for steady gravity currents in shear (e.g., section 5b) and may actually be quite rare in nature, the concept is nevertheless significant because vertical displacements of environmental air are maximized (i.e., optimized) when this configuration is achieved.

A thorough analytic study of the optimal state is presented in section 2. An examination of the steady control-volume vorticity budget for viscous flow yields the same vorticity balance as RKW, $U = \sqrt{2\hat{b}H}$ (section 2c). A flow-force balance analysis based on the (viscous) horizontal momentum equation yields a previously unpublished constraint on the depth of a linear shear layer, $h/H = 3/4$ (section 2d). By then assuming inviscid and adiabatic flow, a unique solution for vertical velocity exiting the domain is derived (section 2e) and a numerical solution for the entire interior flow is obtained (section 2f). The numerical solution demonstrates that the RKW optimal state satisfies the equations of motion everywhere and that the leading edge of the cold pool has a slightly concave shape that is nearly (but not precisely) vertical. We further note (section 2g) that steady inviscid-flow solutions are equally possible under the assumptions of flow separation from the cold pool (advocated by RKW) and no flow separation from the cold pool (advocated by several studies; e.g., Xu 1992); the primary difference in these two viewpoints is the assumption of flow out the top of the control volume (CV) in the former, and flow out the left side of the CV in the latter.

Time-dependent, two-dimensional numerical simulations, designed to evaluate various aspects of the optimal-state concept, are presented in sections 3–6. The control simulation was initialized simply with a stagnant rectangular cold pool and an environment with constant vorticity, along with the constraints determined in the analytic study. A vertically oriented jet emerges from the simulation and remains statistically steady through 3 h of simulation time, despite a few subtle differences from the idealized schematic (e.g., the left side of the jet is turbulent, and some air from the cold pool is drawn upward). The shape of the cold-pool interface is very similar to that determined in the analytic study (specifically the subsection that assumes inviscid flow), that is, the interface has a slightly concave shape and is nearly vertical. Several diagnostics are presented that support the conceptual model of RKW. Most notably, the import of (positive) vorticity on the right side of a control volume

closely matches the generation of (negative) vorticity within the control volume. The flux of vorticity at the top of the control volume, and the net tendency within the control volume, approximately cancel at all times, and both terms oscillate about zero during the simulation; hence the simulated flow is not strictly steady but is statistically steady. Flow within and above the cold pool remains nearly stagnant (relative to the surface gust front) throughout the simulation; decomposition of either the vorticity field or the pressure field shows that this situation arises from cancellation of effects associated with the cold pool and the environmental shear.

Sensitivity experiments are examined in section 5 to test the effects of viscosity and the effects of different initial conditions that do not meet the constraints identified in section 2. It is also demonstrated that lifting of near-surface air is, in fact, optimized in the control simulation. In section 6, different shear profiles are considered; an important conclusion is that the constraint on shear-layer depth compared to the cold-pool depth h/H varies depending on the form of $u(z)$, but that the vorticity balance constraint from RKW [see (14)] does not vary.

The concept of an optimal state for cold pools in shear originally arose from a study of squall lines by RKW. The present study does not address squall lines but rather focuses on the idealized framework of a cold pool in a sheared isentropic environment. Applicability of the concepts and results of this study to more complex phenomenon, like squall lines, awaits further study.

Acknowledgments. We have benefited from discussions on this topic with Joe Klemp, Morris Weisman, Kerry Emanuel, Paul O’Gorman (who motivated the addition of section 6 to this article), and Paul Markowski. We thank the Computational and Information Systems Laboratory (CISL) of NCAR for providing MUDPACK, the multi-grid software for elliptic equations that was used in this study. We also acknowledge high-performance computing support from Yellowstone (ark:/85065/d7wd3xhc), provided by NCAR/CISL, and sponsored by the National Science Foundation.

REFERENCES

- Batchelor, G. K., 1967: *An Introduction to Fluid Dynamics*. Cambridge University Press, 615 pp.
- Benjamin, T. B., 1968: Gravity currents and related phenomena. *J. Fluid Mech.*, **31**, 209–248.
- Davies-Jones, R., and P. Markowski, 2013: Lifting of ambient air by density currents in sheared environments. *J. Atmos. Sci.*, **70**, 1204–1215.
- Durran, D. R., and J. B. Klemp, 1983: A compressible model for the simulation of moist mountain waves. *Mon. Wea. Rev.*, **111**, 2341–2361.
- Jirka, G., and M. Arita, 1987: Density currents or density wedges: Boundary-layer influence and control methods. *J. Fluid Mech.*, **177**, 187–206.
- Ogura, Y., and N. A. Phillips, 1962: Scale analysis of deep and shallow convection in the atmosphere. *J. Atmos. Sci.*, **19**, 173–179.
- Rottman, J. W., J. C. R. Hunt, and A. Mercer, 1985: The initial and gravity-spreading phases of heavy gas dispersion: Comparison of models with phase I data. *J. Hazard. Mater.*, **11**, 261–279.
- Rotunno, R., and J. B. Klemp, 1982: The influence of the shear-induced pressure gradient on thunderstorm motion. *Mon. Wea. Rev.*, **110**, 136–151.
- , and —, 1985: On the rotation and propagation of simulated supercell thunderstorms. *J. Atmos. Sci.*, **42**, 271–292.
- , —, and M. L. Weisman, 1988: A theory for strong, long-lived squall lines. *J. Atmos. Sci.*, **45**, 463–485.
- Saffman, P. G., 1992: *Vortex Dynamics*. Cambridge University Press, 311 pp.
- Shen, Y., and G. Zha, 2010: Improvement of the WENO scheme smoothness estimator. *Int. J. Numer. Methods Fluids*, **64**, 653–675.
- Simpson, J. E., 1997: *Gravity Currents in the Environment and the Laboratory*. 2nd ed. Cambridge University Press, 244 pp.
- Trapp, R. J., and M. L. Weisman, 2003: Low-level mesovortices within squall lines and bow echoes. Part II: Their genesis and implications. *Mon. Wea. Rev.*, **131**, 2804–2823.
- Ungarish, M., 2009: *An Introduction to Gravity Currents and Intrusions*. CRC Press, 489 pp.
- Weisman, M. L., 1992: The role of convectively generated rear-inflow jets in the evolution of long-lived mesoconvective systems. *J. Atmos. Sci.*, **49**, 1826–1847.
- , and R. Rotunno, 2004: “A theory for strong long-lived squall lines” revisited. *J. Atmos. Sci.*, **61**, 361–382.
- , J. B. Klemp, and R. Rotunno, 1988: Structure and evolution of numerically simulated squall lines. *J. Atmos. Sci.*, **45**, 1990–2013.
- Wicker, L. J., and W. C. Skamarock, 2002: Time-splitting methods for elastic models using forward time schemes. *Mon. Wea. Rev.*, **130**, 2088–2097.
- Wyngaard, J. C., 2010: *Turbulence in the Atmosphere*. Cambridge, 393 pp.
- Xu, Q., 1992: Density currents in shear flows—A two-fluid model. *J. Atmos. Sci.*, **49**, 511–524.
- , and M. W. Moncrieff, 1994: Density current circulations in shear flows. *J. Atmos. Sci.*, **51**, 434–446.
- , F.-S. Zhang, and G.-P. Lou, 1992: Finite-element solutions of free-interface density currents. *Mon. Wea. Rev.*, **120**, 230–233.
- , M. Xue, and K. K. Droegemeier, 1996: Numerical simulations of density currents in sheared environments within a vertically confined channel. *J. Atmos. Sci.*, **53**, 770–786.